

The Real-Time Framework for Kinodynamic Planning Applied to Quadrotor Obstacle Avoidance

Ross Allen and Marco Pavone*

The objective of this paper is to present a full-stack, real-time planning framework for kinodynamic robots. This framework is then demonstrated on a quadrotor navigating a dynamic, indoor environment. The proposed framework utilizes an offline-online computation paradigm, neighborhood classification through machine learning, sampling-based motion planning with an optimal cost distance metric, and trajectory smoothing to achieve real-time planning for aerial vehicles. This framework accounts for dynamic obstacles with an event-based replanning structure and a locally reactive control layer that minimizes replanning events. The approach is demonstrated on a quadrotor navigating moving obstacles in an indoor space and stands as, arguably, one of the first demonstrations of full-online kinodynamic motion planning; exhibiting execution cycles of 3 Hz to 5 Hz. For the quadrotor, a simplified dynamics model is used during the planning phase to accelerate online computation. A trajectory smoothing phase, which leverages the differentially flat nature of quadrotor dynamics, is then implemented to guarantee a dynamically feasible trajectory.

I. INTRODUCTION

Due to their ease of use and development along with their wide range of applications in commercial, military, and recreational settings, quadrotor helicopters have become the focus of intense research in the last decade [1, 2, 3]. A standing problem in the field of quadrotor control is the achievement of real-time, high-velocity obstacle avoidance, as conceptually represented in Figure 1. More generally, using the robotic motion planning nomenclature, this problem is referred to as *real-time kinodynamic motion planning* (“kinodynamic” meaning that system dynamics are taken into account during the trajectory planning process), which is an open challenge in robotics; not just quadrotor control [4]. The challenge of real-time kinodynamic planning can be formulated into two questions that serve as the motivation for the work presented in this paper:

Motivating Question 1 Can we develop an algorithm/framework that provides real-time solutions to the kinodynamic planning problem for an arbitrary system?

Motivating Question 2 Given such a generalized approach for kinodynamic planning, can it be shown to work effectively on a real-world, physical system, such as a quadrotor?

In response to such motivating questions, this paper presents a full-stack approach for kinodynamic motion planning which includes: an offline-online computation paradigm, sampling-based optimal motion planning, machine learning of reachable sets, trajectory smoothing, trajectory control, and event-based replanning. To further address the second motivating question we provide validating experiments of a quadrotor navigating static and dynamic obstacles. This is arguably one of the first - if not the first - demonstrations of truly real-time kinodynamic planning on a quadrotor system.

Related Work: Throughout this paper we will detail each component of the full-stack planning framework and discuss its relation to the two motivating questions. First, however, let us build a foundation of prior work that sought to answer similar questions. There are two bodies of complementary, yet distinct, literature that are relevant to the work presented here: those works that address real-time motion planning in a general sense and those that focus on planning and control for quadrotors, specifically. We begin by discussing generalized planning and then move onto quadrotor-specific works.

Frazzoli et. al. provided some of the pioneering work on real-time kinodynamic motion planning [5]. This work implemented the RRT algorithm with node connections achieved by concatenating a small set of motion primitives or

*Department of Aeronautics and Astronautics, Stanford University, Stanford, CA 94305. Email: {rallen10, pavone}@stanford.edu.

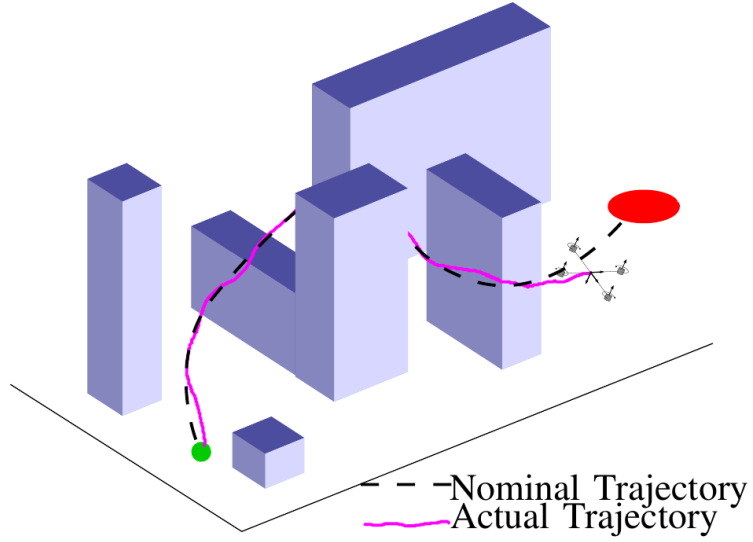


Figure 1. Conceptual diagram of a quadrotor tracking a kinodynamic motion plan through an obstructed environment.

“trim trajectories” between dynamic equilibrium points. Demonstrating on simulations of a small ground robot and a nonlinear helicopter model, the approach was successful in finding feasible trajectories through sparse obstacle sets in 10s of milliseconds. The theory was even applied to dynamic obstacles; however computation times inflated to 10s of seconds. The major shortcoming of this approach is the restrictive nature of “trim trajectories” that prevents the motion planner from achieving *completeness* and is highly reliant on the user to select appropriate motion primitives. For the helicopter example in Frazzoli’s work, only 25 different trim trajectories are used for node connections, all of which being constant speed, level or turning flight. Indeed a helicopter is capable of much more complex maneuvers than those considered. For any given set of motion primitives, it is argued that a pathological obstacle set could be devised that confounds this planning process. This effect is likely to blame for the significant increase in computation time for the dynamic obstacle sets: the motion primitives are “poorly designed” for this specific case. The work presented in our paper does not require the user to select specifically tailored motion primitives, therefore remaining more applicable to arbitrary obstacle sets. Furthermore, it includes a notion of time optimality.

Leven and Hutchinson developed a real-time path planning framework for changing environments [6]. Their framework, which appears to be tailored to multi-link manipulator robots, relied on a *preprocessing phase* that generated a roadmap of the unobstructed configurations space (i.e. configuration space with no obstacles present). It then developed a mapping from nodes in the unobstructed configuration space to discrete cells in the workspace. When the online phase of the planner, referred to as the *query phase*, was initialized and obstacles were introduced, obstructed cells in the workspace could be mapped to corresponding nodes in the configuration space. These nodes were then removed from the roadmap and planning could occur on this augmented roadmap. This approach yielded impressive online planning times of less than one second.

While Leven’s framework is the most similar in form to that presented in our current work - consisting of a framework with offline and online phases to minimize the real-time computations - there are several key differences. Foremost, Leven’s work centered on kinematically-constrained, but not differentially-constrained, robot manipulators. Furthermore they implement a “local planner” that consists of straight-line connections between sampled nodes in the configuration space, thus neglecting some of the kinematic constraints that are fundamental to the manipulators. For the straight-line connection assumption to be valid, they spend considerable time developing a *distance metric* that measures the “closeness” between two configurations. Leven states that the ideal distance metric is swept volume, yet this is too expensive to calculate in real-time so a set of norms in the configuration and workspace are used instead [6]. In our work presented here, we seek to address differentially-constrained systems. To do so we must avoid straight-line approximations for state connections, instead relying on solving an optimal control problem between states (See IV.A). Therefore our distance metric indeed becomes optimal cost. As with Leven’s work, we face the problem that computing optimal cost maybe too expensive to allow real-time computation. To this end we implement a machine-learning algorithm to approximate the optimal cost when real-time calculations are necessary (See IV.B). If our approach were applied to Leven’s work, they could directly estimate swept volume instead of relying on norm-based alternatives.

In the theme of the second motivating question, the most relevant and progressive work in obstacle avoidance and control of quadrotors is, arguably, that of Richter, Bry, and Roy [7, 8]. Relying on foundational work by Mellinger et. al. [9], Richter’s work demonstrated aggressive maneuvers for quadrotors flying in obstructed indoor environments. This was accomplished by generating a set of waypoints through the workspace and then developing a minimum-snap, polynomial trajectory connecting these waypoints. This minimum-snap trajectory produces a “graceful” flight pattern and guarantees dynamic feasibility [9]. Using the differentially flat dynamics of a quadrotor [9], the trajectory polynomials are used to generate analytical expressions for control inputs that are used in a feedforward fashion in the quadrotor flight controller [7].

While Richter’s work represented an important step toward quadrotor planning and control, there remain several critical aspects yet to be achieved. Foremost, the planning algorithm used, RRT* [10], was not implemented in a real-time fashion. The planning phase was accomplished offline, with an a priori map of obstacles. This leaves Richter’s approach unable to handle dynamic obstacles, which is illustrated in their demonstrations that only feature static obstacles. Furthermore, the RRT* algorithm used a simple straight-line metric for the initial planning phase to connect start and goal states; it did not account for the differential motion constraints of the quadrotor [7]. Therefore the initial planning phase produces waypoints that are minimum distance, not necessarily minimum time, to the goal. The snap-minimizing, polynomial trajectories –which guarantee dynamic feasibility– are only produced after the planning phase, implying that the generated trajectory might be significantly suboptimal. The work that is presented in this paper overcomes these shortfalls by employing a *kinodynamic* planner in a truly *real-time* fashion, with obstacle information only available during online execution.

Other works have made significant contributions to the theory of quadrotor control. Sreenath et. al. developed a controller for a quadrotor carrying a cable-suspended load [11]. Hehn and D’Andrea demonstrated stabilization of an inverted pendulum balanced on a quadrotor [3]. Mellinger et. al. devised a hybrid controller capable of perching a quadrotor on an over-vertical surface [12]. While important and impressive in their own right, these works are fundamentally controller designs that wholly neglect motion planning/obstacle avoidance. The work presented in this paper takes kinodynamic planning and flight control as subcomponents of a single problem and proposes a method for addressing both simultaneously.

Several papers have approached the topic of motion planning for quadrotors, even so far as real-time planning. Cowling et. al. [13, 14], and Bouktir et. al. [15] both demonstrate a similar approach that combines trajectory optimization and trajectory control to accomplish high-speed collision avoidance of quadrotors. These papers, however, rely on a mathematically explicit representation of obstacles so that the flight controller can be customized to incorporate these specific obstacles. This limits the approach to a relatively limited number of obstacle configurations that are well defined ahead of time. The approach presented in our paper avoids the explicit mathematical representation of the obstacle space so as to be applicable to virtually any obstacle configuration and does not require obstacle information until online initiation.

Webb and van den Berg made a significant contribution to the field of kinodynamic planning with their development of Kinodynamic RRT* [16]. This work avoided the explicit obstacle representation found in Bouktir et. al. [15] and Cowling et. al. [13, 14] and demonstrated kinodynamic planning for a simulated quadrotor system with linearized dynamics. The Kinodynamic RRT* algorithm is shown to execute in 10s to 100s of seconds; therefore failing to achieve real-time implementation.

An additional, important aspect in this field is validation on a physical system. The papers Frazzoli et. al. [5], Leven and Hutchinson [6], Cowling et. al. [13, 14], Bouktir et. al. [15], Webb and van den Berg [16] only provide simulation results, without a physical demonstration for validation. In contrast Landry produced physical demonstrations of planning and control of a quadrotor navigating a challenging, cluttered environment [17]. Landry’s work, however, is not real-time, as it requires the entire problem to be solved ahead of time before online execution. As with Richter’s work, Landry’s work is, therefore, limited to static obstacles. Grzonka et. al. developed an autonomous quadrotor system capable of navigating highly obstructed indoor environments that executed a variant of the A* algorithm for real-time motion planning [18]. While this work demonstrated real-time planning, the quadrotor was flown at speeds low enough such that differential motion constraints of the quadrotor could be ignored. This implies that the motion planning algorithm demonstrated was in fact geometric and not kinodynamic, leaving it capable of only navigating static or very slow dynamic obstacles. In contrast, our work demonstrates a kinodynamic planner for quadrotor obstacle avoidance capable of navigating high-speed, even adversarial, dynamic obstacles.

This paper is the culmination of the authors’ prior works. In Allen et. al. we introduce the concept of machine learning for rapid estimation of reachable sets for dynamical systems [19]. In our current work we extend this approach to the control-penalized double integrator (see Section IV.A) and show improved estimation accuracy. In Allen and Pavone we first introduce the generalized framework for kinodynamic planning and show how online computation

times can be reduced by several orders of magnitude for simulated systems [20]. The subsequent paper applied the kinodynamic planning framework to a quadrotor robot and demonstrated real-time planning on this physical system [21]. In our current work we extend the real-time framework to dynamic obstacles by developing an effective, event-based replanning scheme. Furthermore we provide extended simulation results to test the framework in a wider variety of obstacle sets than is possible in a laboratory environment, allowing statistical analysis of the framework performance.

Contribution: In the pursuit of addressing the two motivational questions, this work resulted in three key contributions. *Theoretical:* we show that machine learning of reachable sets for dynamical systems is an enabling concept for real-time motion planning. *Practical:* the novel synthesis of existing theoretical results into a coherent, full-stack framework for kinodynamic planning. It is argued that the framework that emerges from this synthesis is greater than the sum of its parts; realizing online planning times for dynamic systems that had yet to be achieved. *Experimental:* arguably the first demonstration of truly real-time planning on a physical quadrotor capable of navigating dynamic, even adversarial, obstacles.

Organization: The paper is structured as follows. Section II gives a formal definition of the kinodynamic planning problem we wish to solve. Section III presents the dynamical model of the quadrotor platform. Section IV develops the real-time kinodynamic planning framework and details how each component of the framework is tailored to the quadrotor system. Section V presents the experimental setup and results, validating the framework. Finally, in Section VI we draw our conclusions and presents directions for future research.

II. PROBLEM STATEMENT

The optimal kinodynamic planning problem consists of the determination of a control function $\mathbf{u}(t) \in \mathbb{R}^m$, and corresponding state trajectory $\mathbf{x}(t) \in \mathbb{R}^n$, that minimize a cost function $\mathcal{J}(\cdot)$ while obeying control constraints, $\mathbf{u}(t) \in \mathcal{U}$, dynamical (differential) constraints, $\mathbf{f}[\dot{\mathbf{x}}(t), \mathbf{x}(t), \mathbf{u}(t), t]$, and state (obstacle) constraints, i.e., $\mathbf{x}(t) \in \mathcal{X}_{\text{free}}(t) \subseteq \mathcal{X}$ (where \mathcal{X} denotes the state space and $\mathcal{X}_{\text{free}}(t)$ is the obstacle-free space which is a function of time to account for moving obstacles). The state at the final time must belong to a given goal region, i.e., $\mathbf{x}(t_{\text{final}}) \in \mathcal{X}_{\text{goal}} \subseteq \mathcal{X}$. Formally, the problem can be posed as a continuous Bolza problem:

Optimal Kinodynamic Planning Problem:

$$\begin{aligned}
 &\text{Find: } \mathbf{u}(t) \\
 &\text{that minimizes: } \mathcal{J}[\mathbf{x}(t), \mathbf{u}(t), t_{\text{final}}] \\
 &\text{subject to: } \mathbf{u}(t) \in \mathcal{U} \quad \forall t \in [t_{\text{init}}, t_{\text{final}}] \\
 &\quad \mathbf{x}(t) \in \mathcal{X}_{\text{free}} \quad \forall t \in [t_{\text{init}}, t_{\text{final}}] \\
 &\quad \mathbf{f}_l \leq \mathbf{f}[\dot{\mathbf{x}}(t), \mathbf{x}(t), \mathbf{u}(t), t] \leq \mathbf{f}_u \quad \forall t \in [t_{\text{init}}, t_{\text{final}}] \\
 &\quad \mathbf{x}(t_{\text{final}}) \in \mathcal{X}_{\text{goal}}
 \end{aligned} \tag{1}$$

where \mathbf{f}_l and \mathbf{f}_u are the lower and upper bounds for the system dynamics described by a differential inclusion (note that, for generality, the dynamics are represented as a differential inclusion even though the quadrotor system discussed later is in fact just an ordinary differential system), t_{init} represents the given, fixed initial planning time, and t_{final} represents the free final time.

Note that if $\mathcal{X}_{\text{free}}(t)$ can be explicitly represented, then the Optimal Kinodynamic Planning Problem may best be solved using existing optimal control methods, similar to what is presented in [22]. However, we are concerned with cases where $\mathcal{X}_{\text{free}}(t)$ is difficult or not even possible to be *explicitly* represented (as is typical for kinodynamic planning problems [23]), and we are only allowed the ability to perform query-based collision checks.

For the quadrotor planning problem discussed in this paper, we choose a minimum-time cost function, that is:

$$\mathcal{J}[\mathbf{x}(t), \mathbf{u}(t), t_{\text{final}}] = t_{\text{final}}. \tag{2}$$

In the following section we specialize the differential constraints, i.e., $\mathbf{f}[\dot{\mathbf{x}}(t), \mathbf{x}(t), \mathbf{u}(t), t]$, to the case of a quadrotor system.

III. QUADROTOR DYNAMICS

III.A. Nonlinear Dynamics

A quadrotor is modeled as an underactuated rigid body where net thrust is constrained along the $-\vec{z}_B$ axis (see Figure 2). The diagram given in Figure 2 represents the relevant coordinate frames and variables for the quadrotor planning and control problem. The world frame, W , is an inertial frame, which is implemented in our case with a North-East-Down (NED) orientation. The body-fixed frame, B , translates and rotates with the quadrotor. The nominal frame, N , is a target frame for trajectory tracking; therefore in perfect trajectory tracking $B = N$. The quadrotor dynamics are given in Eqn. (3) [24]:

$$\begin{aligned}\dot{\vec{\xi}}_B &= \frac{d^W \vec{\xi}_B}{dt}, \\ \ddot{\vec{\xi}}_B &= mg\vec{z}_W - u_1\vec{z}_B, \\ \dot{R}_{BW} &= R_{BW}\hat{\vec{\Omega}}_{BW}, \\ J_B \dot{\vec{\Omega}}_{BW} &= \begin{bmatrix} u_2 \\ u_3 \\ u_4 \end{bmatrix} - \vec{\Omega}_{BW} \times J_B \vec{\Omega}_{BW}.\end{aligned}\quad (3)$$

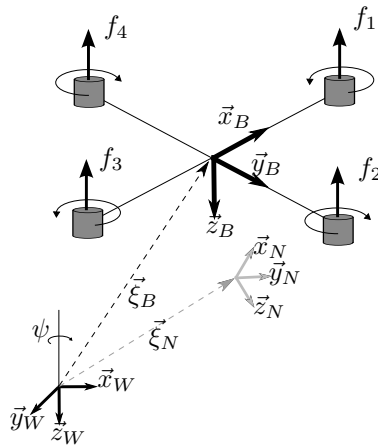


Figure 2. Diagram of quadrotor dynamics with world (inertial), body, and nominal reference frames.

The state vector is given by $\mathbf{x} = [\vec{\xi}_B, \dot{\vec{\xi}}_B, R_{BW}, \vec{\Omega}_{BW}]^T \in \mathbb{R}^9 \times \text{SO}(3)$ where $\vec{\xi}_B$ is the position of the body frame, $\dot{\vec{\xi}}_B$ is the velocity of the body frame, R_{BW} is the rotation matrix from the body frame to the world frame, $\vec{\Omega}_{BW}$ is the angular velocity of the body frame with respect to the world frame, and g is the gravity acceleration. The quadrotor mass is given by m . The control vector is given by $\mathbf{u} = [F_{z_B}, M_{x_B}, M_{y_B}, M_{z_B}] \in \mathbb{R}^4$ where F_{z_B} is the force applied along the body z -axis due to net thrust; and M_{x_B}, M_{y_B} , and M_{z_B} are the moments about the body x , y , and z axes, respectively, due to individual rotor thrusts or torque. Note that $\hat{\cdot}$ denotes the hat-map (i.e., an isomorphism between 3×3 skew-symmetric matrices and vectors in \mathbb{R}^3) [24].

III.B. Approximate Dynamics

There are no known analytical solutions to the minimum-time optimal control problem under the quadrotor's nonlinear dynamics (3). While numerical solutions are possible [20], they are computationally expensive. To minimize online computation times we apply an *approximator-corrector* structure to our framework. The quadrotor is first approximated as a double integrator system, which allows analytical treatment for the *unobstructed* minimal-time control problem (these minimal-time control problems, which are subproblems to the overall planning problem, serve to connect edges in the sampling based planner; see Section IV and IV.A for more details) [16]. At the end of the planning process, the solution trajectory is mapped, or "corrected," back into the fully nonlinear dynamics by leveraging the property of differential flatness (Section IV.E) [9]. The double integrator dynamics are given as

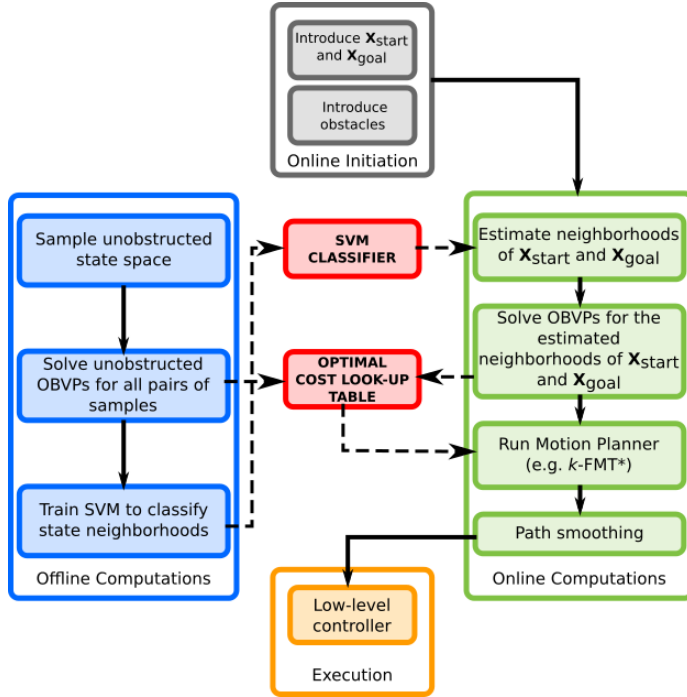


Figure 3. The real-time framework for kinodynamic planning and control.

$$\dot{\mathbf{x}}(t) = A\mathbf{x} + B\mathbf{u} + \mathbf{c}$$

where: $A = \begin{bmatrix} 0 & I \\ 0 & 0 \end{bmatrix}$, $B = \begin{bmatrix} 0 \\ I \end{bmatrix}$, $\mathbf{c} = \begin{bmatrix} 0 \\ g \end{bmatrix}$, $\mathbf{x} = \begin{bmatrix} \vec{\xi}_B \\ \ddot{\xi}_B \end{bmatrix} \in \mathbb{R}^6$, $\mathbf{u} = \ddot{\xi}_B \in \mathbb{R}^3$. (4)

Note that this approximator-corrector approach for the quadrotor dynamics is one of several trade-offs that arise from trying to address, simultaneously, both motivational questions stated in Section I. The framework presented is indeed general enough to accommodate the fully non-linear dynamics of the quadrotor, however, it is desirable to apply an approximation (along with the later correction) to improve online performance during physical demonstrations.

IV. REAL-TIME KINODYNAMIC PLANNING FRAMEWORK

Sampling-based planning algorithms have become the accepted approach for planning in high-dimensional spaces. In a nutshell, the key idea behind sampling-based algorithms is to avoid the explicit construction of the configuration space (which can be prohibitive in complex planning problems) and instead conduct a search that either probabilistically or deterministically probes the configuration space with a sampling scheme. This probing is enabled by a collision detection module, which the motion planning algorithm considers as a “black box” [23]. In this way, a complex trajectory control problem is broken down into a series of many smaller, simpler optimal boundary value problems (OBVP)^a that are subsequently evaluated *a posteriori* for obstacle constraint satisfaction and efficiently strung together into a graph (e.g., tree or roadmap). The primary hurdle for real-time implementability is that without detailed information about a system’s reachability set, a naive sampling-based planner may require the solution to $O(N_s^2)$ OBVPs during online execution, where N_s is the number of sampled states. It is prohibitively expensive to solve such a number of OBVPs in real-time even for the most modestly sized planning problems [28].

^aNote that not all sampling-based planners require the solution to optimal boundary value problems. State space exploration for the RRT algorithm is often achieved by employing a forward dynamic propagator based on randomized or deterministically chosen control inputs [25]. These techniques are prone to “wander” through the state space, lacking the optimality guarantees of algorithms such as RRT*, PRM*, and FMT* [10, 26]. Li et. al. developed the STABLE SPARSE RRT (SST) algorithm that achieves optimality guarantees without requiring OBVP solutions, only a forward dynamic propagator, but execution times for a quadrotor system are on the order of 100s of seconds which is too slow for real-time implementation [27].

To address this we wrap a sampling-based planner in a real-time framework, given in Figure 3, that minimizes the number of OBVPs that need to be solved online. The broad structure of our framework, featuring an offline-online computation paradigm, has similarities to that presented by Leven and Hutchinson [6]. However the details of framework's construction and subcomponents, which are considered a novel contribution of this work, differ significantly from that of Leven's.

The "philosophy" of our framework can be condensed to:

efficiency through machine learning, decision making through optimal control, precomputation when possible.

To elaborate more, the framework (originally proposed in our earlier work [20] and further expanded in [21]) splits computation into offline (Algorithm 1) and online (Algorithm 2) phases. During the offline phase the subroutine `Sample` quasi-randomly draws N_s samples from the continuous state space, without any regard to obstacle locations, which are unknown until online initiation. `SampleData` randomly draws N_{pair} states –with replacement and $N_{\text{pair}} \leq N_s(N_s - 1)$ – from the discrete set of sampled states V , and stores them in two sets A and B . The N_{pair} samples stored in A and B are then paired and OBVPs are solved for each pair; storing the solutions for use during the online phase in a look-up table titled `Cost`. The OBVP solution subroutine, `SolveOBVP`, which is often referred to as a "steering function" in the motion planning literature, is given in Section IV.A. The look-up table `Cost` can equivalently be thought of as a precomputed, unobstructed roadmap (i.e. it is wholly ignorant of obstacle information which is not available until online initiation) through the state space. During the offline phase, a support vector machine (SVM) classifier, referred to as `NearSVM`, is trained using the look-up table `Cost`. The SVM provides query-based estimates of cost-limited reachable sets (i.e., *neighborhoods*) and is discussed in further details in Section IV.B. The cost threshold of the reachable set, often referred to a "neighborhood radius" in the motion planning literature, is the user-defined value J_{th} .

Algorithm 1 Offline Phase for the Kinodynamic Motion Planning Framework

```

1  $V \leftarrow \text{Sample}(\mathcal{X}, N_s)$ 
2  $A \leftarrow \text{SampleData}(V, N_{\text{pair}}, \text{replace})$ 
3  $B \leftarrow \text{SampleData}(V, N_{\text{pair}}, \text{replace})$ 
4  $\text{Cost} \leftarrow \text{SolveOBVP}(A, B)$ 
5  $\text{NearSVM} \leftarrow \text{TrainClassifier}([A, B], \text{Cost}(A, B), J_{\text{th}})$ 

```

At the initiation of the online phase, obstacle data is presented along with the start state, x_{init} , and goal region, $\mathcal{X}_{\text{goal}}$ ^b. A set of N_{goal} states are sampled from the goal region and stored in the discrete set X_{goal} . The SVM classifier is used to rapidly approximate the outgoing neighborhood of x_{init} and the incoming neighborhood of $\mathcal{X}_{\text{goal}}$ among the pre-sampled states; storing the sets in $N_{\text{init}}^{\text{out}}$ and $N_{\text{goal}}^{\text{in}}$, respectively (see Section IV.B for discussion on outgoing and incoming neighborhoods). OBVPs are then solved from x_{init} and $\mathcal{X}_{\text{goal}}$ to their nearest neighbors and the solutions are stored in the look-up table. Note that this reduces the number of online OBVPs solved to $O(1)$!

The sampling-based planner, *kino*-FMT, is then called to return the optimal trajectory through the set of sampled states, V , using the look-up table, or "roadmap", `Cost`. Though many candidate sampling-based planners could be used to compute a trajectory across this roadmap, we rely on the asymptotically-optimal FMT* algorithm for its efficiency (see [26] for a detailed discussion of the advantages of FMT* over state-of-the-art counterparts; see [29] for its kinodynamic extension). The Kinodynamic Fast Marching Trees algorithm (*kino*-FMT) (adapted from [29]) leverages the roadmap to efficiently determine the optimal sequence of sampled states to connect x_{init} and $\mathcal{X}_{\text{goal}}$, performing collision checking in real-time (see Section IV.C).

Finally the sequence of states generated by *kino*-FMT is used as a set of waypoints for a path smoothing algorithm that generates a minimum-snap, dynamically feasible trajectory for the quadrotor (see Section IV.D). Mapping the differentially flat output variables from the smooth trajectory back to the full state and control space (Section IV.E), we can provide feedforward terms to the flight controller (Section IV.F).

To handle dynamic obstacles we must develop a replanning structure that recomputes the kinodynamic motion plan as the environment evolves. We choose to implement an event-based replanner where the existing solution trajectory is continuously checked for collisions with obstacles and replanning is only initiated once the existing plan becomes obstructed. This replanning structure is represented in Figure 4. This event-based replanning is in contrast to a purely time-based, receding horizon replanner more typical for model predictive control. The event-based structure

^bIf this information was available a priori, than all computations could be performed offline and the real-time implementation would become irrelevant.

Algorithm 2 Online Phase for the Kinodynamic Motion Planning Framework

```

1  $X_{\text{goal}} \leftarrow \text{Sample}(\mathcal{X}_{\text{goal}}, N_{\text{goal}})$ 
2  $N_{\text{init}}^{\text{out}} \leftarrow \text{NearSVM}(x_{\text{init}}, V \setminus \{x_{\text{init}}\}, J_{\text{th}})$ 
3  $N_{\text{goal}}^{\text{in}} \leftarrow \text{NearSVM}(V \setminus \{X_{\text{goal}}\}, X_{\text{goal}}, J_{\text{th}})$ 
4 for  $x \in V$  do
5   if  $x \in N_{\text{init}}^{\text{out}}$  then
6     Cost  $\leftarrow \text{SolveOBVP}(x_{\text{init}}, x)$ 
7   if  $x \in N_{\text{goal}}^{\text{in}}$  then
8     Cost  $\leftarrow \text{SolveOBVP}(x, X_{\text{goal}})$ 
9 Path  $\leftarrow \text{kino-FMT}(V, \text{Cost}, x_{\text{init}}, X_{\text{goal}})$ 
10 return SmoothPath(Path)

```

minimizes the number of replanning events which is desirable since even minor communication latency can cause overly aggressive maneuvers when transitioning from one solution trajectory to another; see Section V.C for more discussion.

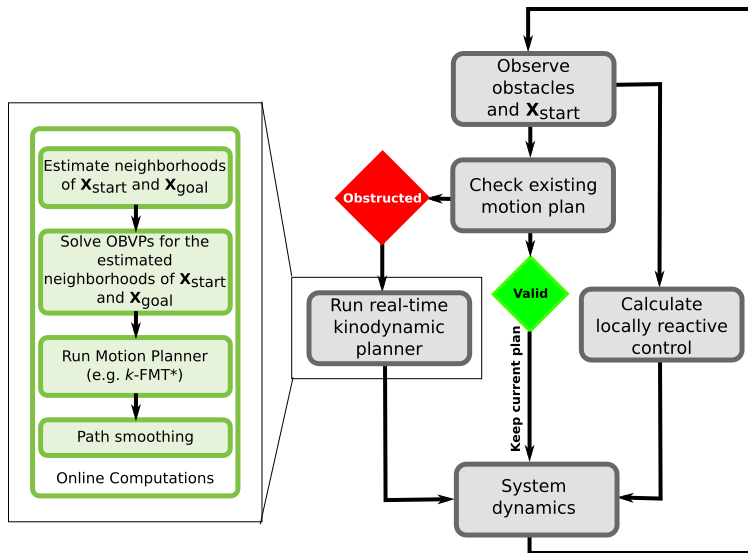


Figure 4. Event-based replanning structure used to account dynamic obstacles.

To further reduce the number of replanning events and provide more "graceful" behavior in proximity to dynamic obstacles we also implement a locally reactive controller. This controller is inspired by the concept of potential fields where nearby obstacles impose a virtual, repelling force on the autonomous system [30]. This reactive controller is represented in Figure 4 and is discussed further in Section IV.F. It is important to note this locally reactive controller is not necessary for the fundamental objective of real-time planning in dynamic environments which is achieved solely based on computation times of the real-time framework. In experimentation, however, it was shown to greatly improve performance, therefore it is discussed in this paper.

We now present the mathematical details for each of the framework components (to make the paper self-contained, we also state a number of results already available in the literature).

IV.A. Analytical Solution to OBVP

In contrast to other works such as Leven and Hutchinson [6] and Richter, Bry, and Roy [7] that use straight line connections between states, we require the solution to an optimal boundary value problem to connect sampled states. As explained in Section II, we minimize computations by approximating our system as the double integrator given in Eqn (4). This approximation enables analytical solutions to the optimal boundary value problem between two sampled states, which is executed in the `SolveOBVP` algorithm. The approximation is corrected for in Section IV.E. The results in this section come from the works [16, 31].

To address control constraints on thrust, a control penalty term is added to the minimum-time cost function, that

is:

$$\mathcal{J}[\mathbf{u}, \tau] = \int_0^\tau 1 + \mathbf{u}[t]^T R_u \mathbf{u}[t] dt, \quad (5)$$

where $R_u \in \mathbb{R}^{m \times m}$ is symmetric positive definite. For a fixed final time, τ , the optimal cost \mathcal{J}^* for the control-penalized double integrator model is given in closed form by Eqn. (6) where $R_u = w_R I$ and w_R is the control penalty weight [16, 31]:

$$\mathcal{J}^*[\tau] = \tau + (\mathbf{x} - \bar{\mathbf{x}}[\tau])^T \mathbf{d}[\tau]. \quad (6)$$

The corresponding control and state trajectories as functions of time t , for a fixed final time τ , are given in Eqn. (7), respectively [16, 31]:

$$\begin{aligned} \mathbf{u}[t] &= R_u^{-1} B^T \exp [A^T(\tau - t)] \mathbf{d}[\tau], \\ \mathbf{x}[t] &= \bar{\mathbf{x}}[t] + G[t] \exp [A^T(\tau - t)] \mathbf{d}[\tau], \end{aligned} \quad (7)$$

where

$$\begin{aligned} \mathbf{d}[\tau] &= G[\tau]^{-1} (\mathbf{x} - \bar{\mathbf{x}}[\tau]), \\ G[t] &= \frac{1}{w_R} \begin{bmatrix} t^{3/3} & 0 & 0 & t^{2/2} & 0 & 0 \\ 0 & t^{3/3} & 0 & 0 & t^{2/2} & 0 \\ 0 & 0 & t^{3/3} & 0 & 0 & t^{2/2} \\ t^{2/2} & 0 & 0 & t & 0 & 0 \\ 0 & t^{2/2} & 0 & 0 & t & 0 \\ 0 & 0 & t^{2/2} & 0 & 0 & t \end{bmatrix}, \\ \bar{\mathbf{x}}[t] &= \exp [At] \mathbf{x}_0 + [0, 0, gt^2/2, 0, 0, gt]^T. \end{aligned} \quad (8)$$

Note that Eqns. (6) and (7) require a *fixed* final time τ . The optimal final time, $\tau^* = \operatorname{argmin} \mathcal{J}[\tau]$, can be solved for via a bisection search of Eqn. (6).

IV.B. Machine Learning of Neighborhoods

When the boundary states, x_{init} and $\mathcal{X}_{\text{goal}}$, are introduced at online initiation they must be connected to the pre-sampled states before the motion planner can execute. Naively connecting the terminal states to all pre-sampled states would require $O(N_s)$ calls to `SolveOBVP`, which is prohibitively many to execute in real-time. Instead we seek to only connect the boundary states with their nearest neighbors, as defined by the cost-limited reachable set (see Figure 5). By limiting edge connections from the boundary states to a fixed number of states in their respective neighborhoods we have effectively reduced the number of online OBVPs to $O(1)$. *This reduction in online OBVPs lies at the core of achieving real-time execution of a kinodynamic planner.*

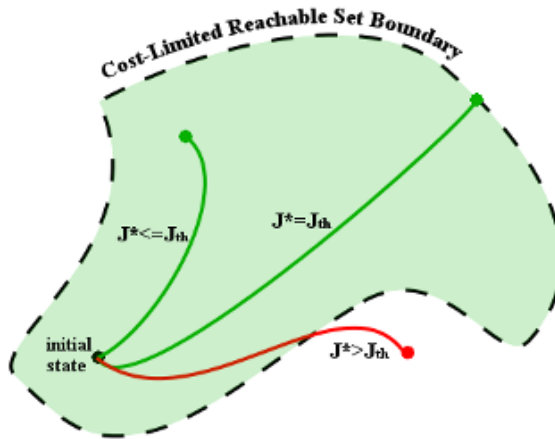


Figure 5. Conceptual representation of a cost-limited reachable set for a notional 2D dynamical system. Formally, a (forward) cost-limited reachable set is the set of states that can be reached from a given state with a cost bounded above by a given threshold (denoted as J_{th}).

A conceptual diagram of a cost-limited reachable set, i.e. *neighborhood*, of a given state is represented in Figure 5. The mathematical definition of the “outgoing neighborhood” or *forward* cost-limited reachable set of a state \mathbf{x}_a is:

$$R^{\text{out}}(\mathbf{x}_a, \mathcal{U}, J_{\text{th}}) := \{\mathbf{x}_b \in \mathcal{X} \mid \exists \mathbf{u} \in \mathcal{U} \text{ and } \exists t' \in [t_0, t_f] \text{ s.t. } \mathbf{x}(t') = \mathbf{x}_b \text{ and } \mathcal{J}^* \leq J_{\text{th}}\}, \quad (9)$$

where J_{th} is a user-defined cost threshold. In plain English, the forward reachable set is the union of all states $\mathbf{x}_b \in \mathcal{X}$ such that the optimal cost, \mathcal{J}^* , to steer the system from \mathbf{x}_a to \mathbf{x}_b is less than the cost threshold J_{th} . Also of importance is the concept of an “incoming neighborhood” or backward reachable set. The backward reachable set of state \mathbf{x}_b is the union of all states, \mathbf{x}_a , such that \mathbf{x}_b is in the forward reachable set of \mathbf{x}_a .

In general the determination of reachability sets is a computationally-expensive problem [32], therefore the real-time planning framework applies an approximation to the reachable sets based on machine learning. During the offline phase a support vector machine (SVM) is trained with data stored in `Cost` and provides a query-based classification of nearest neighbors. This approach leverages the authors’ prior work [19], which demonstrated the accuracy and efficiency of this procedure for a number of nonlinear dynamical systems.

To elaborate, we seek a function that makes a simple, binary discrimination:

is the optimal cost to traverse from an arbitrary state \mathbf{x}_a to an arbitrary state \mathbf{x}_b less than a given threshold J_{th} , or not?

To develop such a function, we leverage the data in `Cost` to provide *training examples*. A training example consists of a initial state \mathbf{x}_a , final state \mathbf{x}_b , and optimal cost of traversal between the two. For each training example $i = 1, \dots, N_{\text{train}}$ where $N_{\text{train}} \leq N_{\text{pair}}$, the initial and final states are concatenated into an attribute vector $\mathbf{p}^{(i)}$. If the optimal cost of the training example is less than the user-defined threshold, J_{th} , then it is given a label $y^{(i)} = +1$; otherwise it is given label $y^{(i)} = -1$. The training of the SVM is accomplished with the optimization given in Eqn. (10) [33]:

$$\begin{aligned} & \underset{\alpha}{\text{maximize}} \quad \sum_{i=1}^{N_{\text{train}}} \alpha_i - \frac{1}{2} \sum_{i,j=1}^{N_{\text{train}}} y^{(i)} y^{(j)} \alpha_i \alpha_j K(\mathbf{p}^{(i)}, \mathbf{p}^{(j)}) \\ & \text{subject to} \quad 0 \leq \alpha_i \leq C, \quad i = 1, \dots, N_{\text{train}} \\ & \quad \sum_{i=1}^m \alpha_i y^{(i)} = 0 \end{aligned} \quad (10)$$

where the α_i ’s are Lagrange multipliers, C is a user-defined parameter that relaxes the requirement that the training examples be completely separable, and $K(\cdot)$ is the kernel function. The vectors corresponding to non-zero Lagrange multipliers α_i ’s are the *support vectors*. For this work the *kernel function*, K , has the form

$$K(\mathbf{p}^{(1)}, \mathbf{p}^{(2)}) = \left(\phi(\mathbf{p}^{(1)})^T \phi(\mathbf{p}^{(2)}) + c \right)^p,$$

where ϕ is a nonlinear mapping of the attribute vector to a *feature vector* (see Table 4 for an example of feature vector used in this work), c is a weighting parameter between first and second order terms, and p is kernel order chosen by the user. Once the support vectors are obtained, predictions on reachability for a new OBVP, paramaterized by $\tilde{\mathbf{p}}$, can be made with the predictor

$$\text{sgn} \left(\sum_{i=1}^{N_{\text{train}}} \alpha_i y^{(i)} K(\mathbf{p}^{(i)}, \tilde{\mathbf{p}}) + b \right). \quad (11)$$

where b is a bias term that is determined as a function of the Lagrange multipliers [33].

To contrast this approach with that of prior literature, Leven and Hutchinson’s used a set of norms in the work space and configuration space as a rough surrogate for their desired distance metric of swept volume [6]. If our machine learning approach were applied to the work in [6], swept volume reachable sets could be directly approximated instead of having to devise a surrogate function. This allows the flexibility in our framework to be applied to a more general set of planning problems.

Note that `NearSVM` is trained on data in `Cost` which is generated with no knowledge of obstacle placement. Therefore, `NearSVM` has no function in predicting obstacle collisions. Collision checking is solely within the realm of the sampling-based planner discussed in Section IV.C. Results on training and testing of the SVM classifier for a quadrotor system are presented in Section V.E.

IV.C. Sampling-Based Planner

The sampling-based motion planner at the core of our real-time framework is a kinodynamic variant of the Fast Marching Tree (FMT*) algorithm [26], and is presented in pseudo-code in Algorithm 3. The algorithm works by expanding a tree, stored in a set of edge connections E , along the minimum cost-to-come front through the pre-sampled set of states V . The frontier of the tree is stored in set H and unconnected samples are stored in set W .

For each iteration of the algorithm, the minimum cost-to-come sample z is used as a pivot for exploration. The forward-reachable set of z among the sampled states V is stored in the discrete set N_z^{out} . The intersection of N_z^{out} and set W is determined and the result is stored in set X_{near} . Each sample, $x \in X_{near}$, represents a candidate for expansion of the tree. For each candidate x the backward reachable set among sampled states is determined and saved as set N_x^{in} . The set Y_{near} is determined as the intersection of H and the backward reachable set of x , N_x^{in} . The sample $y_{min} \in Y_{near}$ represents the optimal connection point (assuming no obstacles) between x and the existing tree. If the connection from y_{min} to x is free of collisions with obstacles, then the (y_{min}, x) edge is added to the tree, x is added to the frontier set H and removed from W . Once all nodes in X_{near} are analyzed, the pivot node z is removed from the frontier set and the process is repeated. The algorithm succeeds in finding a path from x_{init} to \mathcal{X}_{goal} as soon as the current pivot, z , is an element of \mathcal{X}_{goal} . If the frontier set H ever becomes empty, then *kino*-FMT reports failure. The (asymptotic) optimality properties of FMT* (and its kinodynamic variants) are discussed in [26, 34, 29].

Algorithm 3 Kinodynamic Fast Marching Tree Algorithm (*kino*-FMT)

```

1  $V \leftarrow V \cup \{x_{init}\} \cup \{X_{goal}\}$ 
2  $E \leftarrow \emptyset$ 
3  $W \leftarrow V \setminus \{x_{init}\}; H \leftarrow \{x_{init}\}$ 
4  $z \leftarrow x_{init}$ 
5 while  $z \notin \mathcal{X}_{goal}$  do
6    $N_z^{out} \leftarrow \text{Near}(z, V \setminus \{z\}, J_{th})$ 
7    $X_{near} = \text{Intersect}(N_z^{out}, W)$ 
8   for  $x \in X_{near}$  do
9      $N_x^{in} \leftarrow \text{Near}(V \setminus \{x\}, x, J_{th})$ 
10     $Y_{near} \leftarrow \text{Intersect}(N_x^{in}, H)$ 
11     $y_{min} \leftarrow \arg \min_{y \in Y_{near}} \{\text{Cost}(y, T = (V, E)) + \text{Cost}(\overline{yx})\}$ 
12    if CollisionFree( $y_{min}, x$ ) then
13       $E \leftarrow E \cup \{(y_{min}, x)\}$ 
14       $H \leftarrow H \cup \{x\}$ 
15       $W \leftarrow W \setminus \{x\}$ 
16     $H \leftarrow H \setminus \{z\}$ 
17    if  $H = \emptyset$  then
18      return Failure
19     $z \leftarrow \arg \min_{y \in H} \{\text{Cost}(y, T = (V, E))\}$ 
20 return Path( $z, T = (V, E)$ )

```

IV.D. Minimum-Snap Trajectory Smoother

Trajectory smoothing is commonly implemented in motion planning to improve the quality of the trajectory returned by the planner. Furthermore, in our case, we need to correct for the double integrator approximation previously made. To this end we improve the sampling-based planner's solution computed via *kino*-FMT by connecting the solution samples with a high-order polynomial spline. Building on Mellinger's work [9], Richter et. al. [7] formulate the spline determination as an unconstrained quadratic programming problem that minimizes the integral of the square of the snap (i.e. the 4th derivative of position); see Eqn. (12). In the unconstrained formulation, derivatives at samples of the motion plan, i.e. waypoints, are left as free parameters for optimization. For completeness we present the essential results of Richter as they are used in our current approach [7, 8].

Our goal in this section is to determine the coefficients of M polynomials of order N . These polynomials form a spline that is continuous up to the 4th derivative and passes through the sampled states, or "nodes", of the solution trajectory determined in Section IV.C. While an infinite number of splines may exist that satisfy these conditions, we seek the spline that minimizes the integral of the square of the snap. Let us begin by considering a single polynomial

$P(t) = \sum_{n=0}^N p_n t^n$. The minimum-snap cost function for a single polynomial is defined as

$$J_{\text{snap}} = \int_0^T P^{(4)}(t)^2 dt = \mathbf{p}^T Q(T) \mathbf{p}, \quad (12)$$

where $Q(T)$ is the Hessian matrix of J_{snap} with respect to the polynomial coefficients, \mathbf{p} is a vector of the $N + 1$ polynomial coefficients, and T is the polynomial segment time which is determined by the kinodynamic planner. The superscript (4) implies the 4th derivative of the polynomial. Without derivation, the Hessian matrix is given as^c

$$\begin{aligned} Q_{i,j}(T) &= 2 \left(\prod_{k=0}^3 (i-k)(j-k) \right) \frac{T^{i+j-7}}{i+j-7} \quad \text{for: } i \geq 4 \wedge j \geq 4, \\ Q_{i,j}(T) &= 0 \quad \text{otherwise.} \end{aligned} \quad (13)$$

As previously mentioned, the polynomial is constrained at its terminal points, $t = 0$ and $t = T$, to the waypoints of the motion plan determined in Section IV.C. The derivatives of the polynomial at its terminal points can be fixed or left as free parameters for optimization. Even as free parameters, however, the derivatives must satisfy continuity between polynomials in the spline. These constraints can be encoded as the linear function

$$A\mathbf{p} = \mathbf{d} \quad (14)$$

$$A = \begin{bmatrix} A_0 \\ A_T \end{bmatrix}, \quad \mathbf{d} = \begin{bmatrix} \mathbf{d}_0 \\ \mathbf{d}_T \end{bmatrix} \quad (15)$$

where the terms are given as

$$A_{0_{i,j}} = \begin{cases} \prod_{k=0}^{i-1} (i-k) & \text{if } i = j \\ 0 & \text{if } i \neq j \end{cases} \quad (16)$$

$$\mathbf{d}_{0_i} = P^{(i)}(0) \quad (17)$$

$$A_{T_{i,j}} = \begin{cases} \left(\prod_{k=0}^{i-1} (i-k) \right) T^{i-j} & \text{if } i \geq j \\ 0 & \text{if } i < j \end{cases} \quad (18)$$

$$\mathbf{d}_{T_i} = P^{(i)}(T) \quad (19)$$

Numerical stability can be achieved by reformulating the constrained problem represented in Eqns. (12) and (15) as an unconstrained optimization [7, 8]. This is achieved by optimizing over the polynomial derivatives at the terminal points instead of the polynomial coefficients. Under this reformulation, Eqns. (12) and (15) become

$$J_{\text{snap}} = \mathbf{d}^T A^{-T} Q(T) A^{-1} \mathbf{d}, \quad (20)$$

and the polynomial coefficients are determined, a posteriori, via inversion of Eqn. (14).

Now that we have formulated the optimization problem for a single polynomial, we must consider the optimization over the spline of M polynomials. To this end we form $A_{1\dots M}$ and $Q_{1\dots M}$ which are block diagonal matrices composed of the A and Q matrices for each segment. We could also simply concatenate the derivative vectors into a vector $\mathbf{d}_{1\dots M}$, however it is desirable to separate this vector into components that are fixed and those that are free parameters of optimization. Therefore the derivative vector for the spline optimization is formed as

$$\mathbf{d}_{\text{total}} = \begin{bmatrix} \mathbf{d}_{\text{fix}} \\ \mathbf{d}_{\text{free}} \end{bmatrix}. \quad (21)$$

With this reordering of the derivative vector in Eqn. (21), an ordering matrix C is required that preserves the proper relationships with the block matrices $A_{1\dots M}$ and $Q_{1\dots M}$. Furthermore, the ordering matrix C also encodes the enforcement of continuity of derivatives at intermediate waypoints. Now the minimum-snap cost function for the entire spline is given as

$$J_{\text{snap}} = \mathbf{d}_{\text{total}}^T C A_{1\dots M}^{-T} Q_{1\dots M} A_{1\dots M} C^T \mathbf{d}_{\text{total}}. \quad (22)$$

^cNote that we diverge from Richter by only considering the minimization on the 4th derivative, where Richter leaves the formulation more general as a weighted sum of squares of derivatives. Furthermore, due to the fact that Richter uses a geometric planner to determine waypoints, his approach requires a time allocation optimization to determine polynomial segment times, T [7, 8]. In contrast, our work determines the polynomial segment times during the time-minimizing kinodynamic planning; see Section IV.C.

For simplicity, define the matrix $H = CA_{1\dots M}^{-\top} Q_{1\dots M} A_{1\dots M} C^\top$ and partition it such that Eqn. (22) can be written

$$J_{\text{snap}} = \begin{bmatrix} \mathbf{d}_{\text{fix}} \\ \mathbf{d}_{\text{free}} \end{bmatrix}^\top \begin{bmatrix} H_{11} & H_{12} \\ H_{21} & H_{22} \end{bmatrix} \begin{bmatrix} \mathbf{d}_{\text{fix}} \\ \mathbf{d}_{\text{free}} \end{bmatrix}. \quad (23)$$

Differentiating and setting to zero solves for the free derivatives at the waypoints

$$\mathbf{d}_{\text{free}}^* = -H_{22}^{-1} H_{12}^\top \mathbf{d}_{\text{fix}}. \quad (24)$$

Now that the derivatives at each waypoint are determined, the polynomial coefficients can be determined by inverting Eqn. (14). This process is applied for the determination of four splines: x, y, and z positions and yaw. These splines correspond to the differential flat output variables discussed in Section IV.E.

It is important to note here that once smoothing is applied, the trajectory is no longer guaranteed to be collision free. Therefore it is necessary to perform an additional collision checking phase during the trajectory smoothing phase. If one of the polynomials in the spline is found to collide with an obstacle, then a new smoothed trajectory must be determined. This is accomplished by sampling the midpoint of the underlying motion plan solution which is guaranteed to be collision free (else it would have not been selected as a valid motion plan). The trajectory smoother than solves the minimum-snap optimization problem for $M+1$ trajectory segments. This is repeated until the smoothed trajectory is collision free. See Richter et. al. for more details [7, 8].

IV.E. Differentially Flat Mapping

The trajectory smoother from Section IV.D produces polynomial splines for position and yaw that are continuous up to their fourth derivative. Mellinger et. al. showed that the state and control variables for the nonlinear quadrotor dynamics can be expressed in terms of $\vec{\xi}_N$ and $\dot{\psi}_N$ and their derivatives up to fourth order; thus proving Eqn. (3) represents a differentially flat system with flat output variables $\vec{\xi}_N$ and $\dot{\psi}_N$ [9]. This mathematical property proves that the smoothed trajectory from Section IV.D is guaranteed to be dynamically feasible for the quadrotor; therefore correcting the double-integrator approximation made to solve the planning problem. For completeness we state the results of Mellinger et. al. for the mapping from the flat outputs to the nominal state and control variables. Note that, while the following equations are taken almost directly from [9], there are some subtle coordinate frame changes.

The nominal position and velocity state variables are identically $\vec{\xi}_N$ and $\dot{\vec{\xi}}_N$, respectively. The thrust control variable is given as

$$u_{1ff} = -\vec{z}_B \cdot \vec{F}_N, \quad \text{where: } \vec{F}_N = m\ddot{\vec{\xi}}_N - mg\vec{z}_W \quad (25)$$

The subscript ff indicate that this thrust value appears as a feedforward term in the flight controller (Section IV.F). The nominal orientation matrix is given by the nominal frame axes represented in world coordinates:

$$\vec{R}_N = [{}^W\vec{x}_N, {}^W\vec{y}_N, {}^W\vec{z}_N], \quad (26)$$

where

$$\begin{aligned} \vec{z}_N &= -\frac{\vec{F}_N}{\|\vec{F}_N\|} \\ \vec{y}_S &= [-\sin\psi_N, \cos\psi_N, 0]^\top \\ \vec{x}_N &= \frac{\vec{y}_S \times \vec{z}_N}{\|\vec{y}_S \times \vec{z}_N\|} \\ \vec{y}_N &= \vec{z}_N \times \vec{x}_N. \end{aligned} \quad (27)$$

The nominal angular velocity vector is given by

$$\vec{\Omega}_{NW} = p_N \vec{x}_N + q_N \vec{y}_N + r_N \vec{z}_N \quad (28)$$

where the individual components of nominal angular velocity are

$$\begin{aligned} p_N &= -\vec{h}_\Omega \cdot \vec{y}_N \\ q_N &= \vec{h}_\Omega \cdot \vec{x}_N \\ r_N &= \dot{\psi}_N \vec{z}_W \cdot \vec{z}_N \end{aligned} \tag{29}$$

For compactness we have defined

$$\vec{h}_\Omega = \frac{m}{u_{1ff}} \left((\vec{\xi}_N^{(3)} \cdot \vec{z}_N) \vec{z}_N - \vec{\xi}_N^{(3)} \right) \tag{30}$$

The nominal angular acceleration, used in the calculation of the feedforward moment terms, is derived to be

$$\dot{\vec{\Omega}}_{NW} = \alpha_{1N} \vec{x}_N + \alpha_{2N} \vec{y}_N + \alpha_{3N} \vec{z}_N \tag{31}$$

where the individual components of nominal angular acceleration are

$$\begin{aligned} \alpha_{1N} &= -\vec{h}_\alpha \cdot \vec{y}_N \\ \alpha_{2N} &= \vec{h}_\alpha \cdot \vec{x}_N \\ \alpha_{3N} &= (\ddot{\psi}_N \vec{z}_N - \dot{\psi}_N \vec{h}_\Omega) \cdot \vec{z}_W \end{aligned} \tag{32}$$

Again for compactness we give

$$\begin{aligned} \vec{h}_\alpha &= -\frac{1}{u_{1ff}} \left(m \vec{\xi}_N^{(4)} + \ddot{u}_{1ff} \vec{z}_N + 2\dot{u}_{1ff} \vec{\Omega}_{NW} \times \vec{z}_N \right. \\ &\quad \left. + \vec{\Omega}_{NW} \times \vec{\Omega}_{NW} \times \vec{z}_N \right) \end{aligned} \tag{33}$$

The derivative of the net thrust, which appear in Eqn (33), are derived to be

$$\begin{aligned} \dot{u}_{1ff} &= -m \vec{\xi}_N^{(3)} \cdot \vec{z}_N \\ \ddot{u}_{1ff} &= - \left(m \vec{\xi}_N^{(4)} + \vec{\Omega}_{NW} \times \vec{\Omega}_{NW} \times \vec{z}_N \right) \cdot \vec{z}_N \end{aligned} \tag{34}$$

Note that the equations presented in this section are taken almost directly from Mellinger et. al. [9] but are stated here for completeness of our approach.

IV.F. Flight Controller

The flight controller synthesizes work by Lee et. al. [24] with Ge and Cui [30] and is composed of three parts: a feedforward component, a feedback component, and a "locally reactive" component. Feedforward inputs, denoted with subscript *ff*, are generated from the differentially flat mapping in Section IV.E and feedback terms, denoted with subscript *fb*, are generated via proportional-derivative (PD) tracking of position, velocity, orientation and angular velocity. The locally reactive terms, denoted with subscript *lr*, are loosely based on the concept of potential fields where proximity to obstacles create a virtual force to "push" the quadrotor away (i.e. the quadrotor reacts to obstacles). The reactive terms were originated from Ge and Cui's work, but were modified during experimentation until a desirable behavior was observed. Since these terms were empirically derived, they no longer represent a gradient of a potential field. As previously noted, the locally reactive terms of the controller are not necessary to achieve real-time obstacle avoidance as the planning framework is fast enough to account for dynamic obstacles on its own. During flight tests, however, the locally reactive controller terms significantly improved the performance of the quadrotor by generating more predictable, graceful maneuvers. Equation (35) gives the net thrust control input due to the feedforward, feedback, and locally reactive components.

$$\begin{aligned} u_1 &= u_{1ff} + u_{1fb} + u_{1lr} \\ &= -\vec{z}_B \cdot \left(\vec{F}_{ff} + \vec{F}_{fb} + \vec{F}_{lr} \right) \\ &= -\vec{z}_B \cdot \left(m \ddot{\vec{\xi}}_N - mg \vec{z}_W + K_\xi \vec{e}_\xi + K_v \vec{e}_v + \vec{F}_{lr} \right) \end{aligned} \tag{35}$$

Equation (36) presents the control inputs for the moments about the body axes.

$$\begin{aligned}[u_2, u_3, u_4]^T &= [u_2, u_3, u_4]_{ff}^T + [u_2, u_3, u_4]_{fb}^T \\ &= J_B \left(R_B^T R_N \dot{\vec{\Omega}}_{BW} - \vec{\Omega}_{BW} \times (R_B^T R_N \vec{\Omega}_{BW}) \right) \\ &\quad + \vec{\Omega}_{BW} \times J_B \vec{\Omega}_{BW} + K_R \vec{e}_R + K_\Omega \vec{e}_\Omega\end{aligned}\tag{36}$$

The error terms for feedback control are given by Eqn. (37) [24]

$$\begin{aligned}\vec{e}_\xi &= \vec{\xi}_N - \vec{\xi} \\ \vec{e}_v &= \dot{\vec{\xi}}_N - \dot{\vec{\xi}} \\ \vec{e}_R &= \frac{1}{2} (R_D^T R_D - R_D^T R_B)^\vee \\ \vec{e}_\Omega &= R_B^T R_D \vec{\Omega}_D - \vec{\Omega}_B\end{aligned}\tag{37}$$

where \vee represents the *vee-map*; the inverse of the *hat-map*. The matrices $K_\xi, K_v, K_R, K_\Omega \in \mathbb{R}^{3 \times 3}$ are user-defined gain matrices for PD trajectory tracking.

The rotation matrix R_D represents the *desired* orientation to account for feedback and locally reactive terms. This is distinct from the nominal orientation R_N that is independent of feedback and obstacle influence. During perfect trajectory tracking with no nearby obstacles we have $R_N = R_D = R_B$. The rotation matrix R_D is calculated by substituting $\vec{F}_{ff} + \vec{F}_{fb} + \vec{F}_{lr}$ into Equation 25 and proceeding with Equations 26 and 27.

The locally reactive force term, \vec{F}_{lr} , in Equation 35 is calculated based on obstacle proximity and velocity via

$$\vec{F}_{lr} = \sum_{i=1}^{n_{obs}} \frac{1}{||\vec{r}_i||^2} (-\eta_r \hat{n}_i + \eta_{va} v_{n_i} \hat{n}_i - \eta_{vp} v_{n_i} (v_{n_i} \hat{n}_i - \vec{v}_i))\tag{38}$$

where n_{obs} is the number of obstacles, \vec{r}_i is the position of the closest point on the i^{th} obstacle with respect to the quadrotor body frame, \hat{n}_i is the unit vector in the \vec{r}_i direction, \vec{v}_i is the relative velocity of the i^{th} obstacle with respect to the quadrotor, and $v_{n_i} = \vec{v}_i \cdot \hat{n}_i$. The first two terms in Equation 38 represents a repulsive force due to obstacle relative position and velocity, respectively. The third term is a steering term due to obstacle relative velocity. The variables η_r , η_{va} , and η_{vp} are weighting factors for position, aligned velocity, and perpendicular velocity, respectively. For obstacles outside of a user-defined influence region, the locally reactive force in Equation 38 is set to zero. Furthermore, if $v_{n_i} < 0$ then the velocity terms of Equation 38 are set to zero. It should be again noted that this locally reactive control is non-essential for addressing the motivating questions in Section I; however it improves performance during physical demonstrations by minimizing the number of replanning events necessary by avoiding occlusion of the existing motion plan. Distinguishing the locally reactive control as non-essential is important because it does require additional obstacle information that is not required by the rest of the framework (i.e. position and velocity data for each obstacle as opposed to just collision detection). Therefore, if we want to be more strict with our assumptions of obstacle data, we could eliminate the locally reactive control without sacrificing the real-time planner as a whole.

V. EXPERIMENTAL VALIDATION

We validate the real-time framework in both simulation and physical experiments. In this section we describe the results of these test campaigns.

V.A. Simulated Results

While physical demonstrations are the ultimate test of the framework's effectiveness, limited laboratory space constrains the number and complexity of obstacles sets that can be tested. Therefore a simulation with a maze of obstacles is devised to validate our approach in more complex environments. The simulated environment consists of a corridor with dimensions $20\text{m} \times 4\text{m} \times 4\text{m}$ with the start and goal states randomly generated from opposing ends of the corridor. Cuboid obstacles are arranged to create a 3-dimensional "maze". A fixed number of spherical obstacles with radii of one meter are placed at random to ensure that we have not inadvertently tailored our algorithm to this

specific cuboid-maze obstacle set^d. Figure 6 gives an instance of this obstacle configuration and associated solution. The start state is shown on the left side of the image and the goal state is obscured by the final obstacle on the right. The initial motion plan, as returned by *kino*-FMT (see Sections IV.A and IV.C), is indicated in blue and the smoothed, dynamically feasible trajectory (see Section IV.D) is indicated in multicolor.

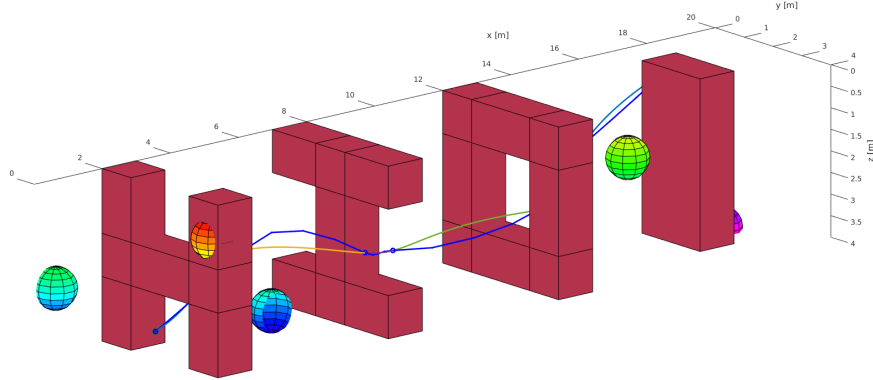


Figure 6. A instance of one of the simulated flight tests with a 3D maze of wall structures and randomly placed spherical obstacles.

The primary performance metrics of the real-time planning framework are considered the online computation time, solution cost, failure rate, and classification accuracy of reachable sets by the machine learning algorithm. Here we discuss the performance in terms of computation time, solution cost, and failure rate; saving discussion of the machine learning performance for Section V.E.

Through the simulated test campaign it was determined that the performance metrics were most dependent upon two *design variables*: number of sampled states and number of terminal state neighbor connections; and a third, situation-dependent variable: obstacle coverage. The simulated test campaign involved selecting values for the design variables and executing 100 trials for each combination. For each trial the start state, goal state, and spherical obstacle placement were randomized. We summarize the trade-offs between design variables and performance metrics in Table 1.

Table 1. Trajectory cost and computation time breakdown for the Real-Time Kinodynamic Framework for a range of design variables

Design Variables		Performance Metrics	
	# Terminal State Neighbors	Avg. Trajectory Cost [s]	Avg. Computation Time [s]
# Samples			
Fixed Numbers	150	8.91	0.060
	250	8.16	0.067
	500	7.35	0.110
	1000	7.14	0.280
	2000	7.05	0.985
	3000	6.95	2.289
Fixed Ratios	150	8.58	0.065
	250	7.85	0.081
	500	6.79	0.154
	1000	6.33	0.394
	2000	5.91	1.268
	3000	5.80	2.632

Figures 7 and 8 illustrate the trends of performance metrics as functions of the design variables. As expected, with increasing number of samples N_s , the solution cost, \mathcal{J} , decreases while computation time increases. Based on Figure 7, we can see that $N_s = 500$ is an acceptable sample density for this obstacle configuration as there is marginal

^dNote that the framework developed in section IV is in no way restricted to cuboid and spherical obstacles. For implementation, however, we choose relatively simplistic obstacles because the development of sophisticated collision checking routines is outside the scope of this paper

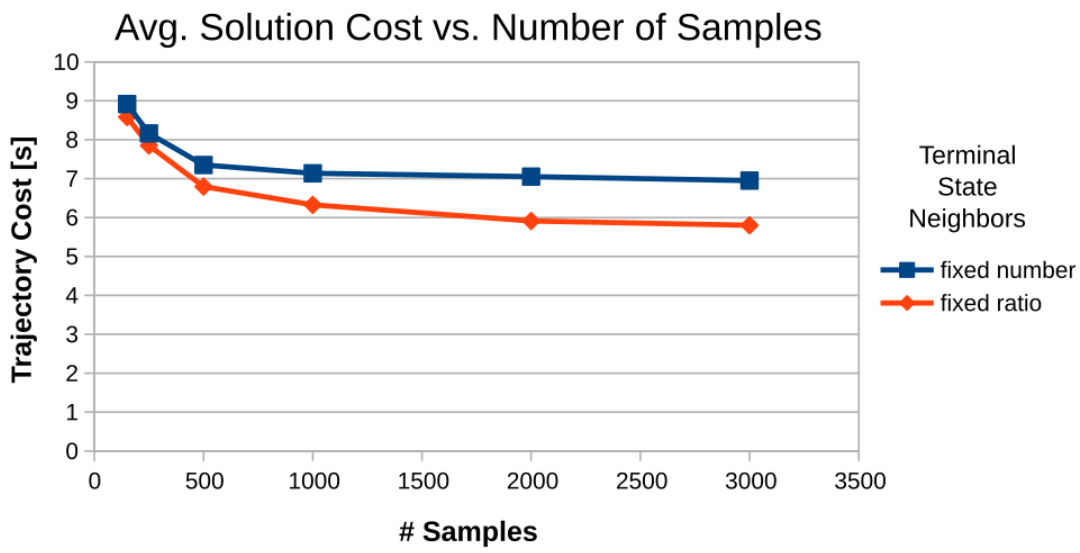


Figure 7. Average trajectory cost as a function of number of state samples and number of terminal state neighbors for a fixed obstacle coverage.

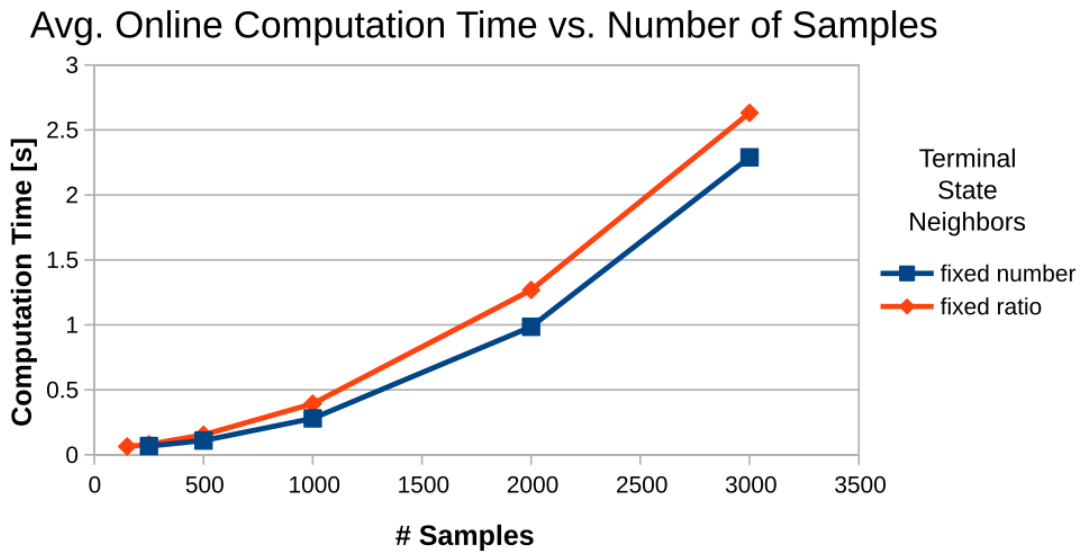


Figure 8. Average online computation time as a function of number of state samples and number of terminal state neighbors for a fixed obstacle coverage.

decrease in solution cost for higher sample numbers. As shown in Table 1, 500 samples corresponds to an average solution time of 0.110 seconds for a fixed number of terminal state neighbors and 0.154 seconds for a fixed ratio of terminal state neighbors. It is argued that these computation times represent ‘real-time’ planning; we verify this claim with physical demonstrations in Section V.C and compare to computation times in the existing literature in Section V.D.

The effect of neighborhood sizes for the terminal states (i.e. the number of states in the pre-sampled set V for which connections are made to the start and goal states) is also presented in Figures 7 and 8. For the fixed number of terminal state neighbors, the start and goal states are connected to the precomputed roadmap at the 10 closest states in the set of pre-sampled states, V ; where closeness is approximated by the machine learning algorithm. For the fixed ratio of terminal state neighbors, the start and goal states are connected to the closest 10 percent of the set V . Each connection between the terminal states and the precomputed roadmap constitutes an online OBVP solution; therefore the fixed number corresponds to $\mathcal{O}(1)$ online OBVPs, where the fixed ratio corresponds to $\mathcal{O}(N_s)$ online OBVPs.

This comparison of number of terminal state neighbors is made to determine the effect of restricting the online OBVP solutions to constant order, which is argued to be an enabling technique for real-time kinodynamic planning. From Figure 8 we see that, indeed, restriction of terminal state neighbors leads to a reduction in online computation time of up to 15%. While 15% is not a staggering difference in computation time, it is important to note that this is only representative of the quadrotor system where much work has been done to minimize the computation time for OBVPs (see Section IV.A). For more general systems where OBVPs may be very computationally expensive, this restriction to $\mathcal{O}(1)$ online OBVPs may reduce online planning times by several orders of magnitude [19]. The decrease in computation time, however, comes at the expense of increased solution cost as indicated by Figure 7.

Another insightful question is, *for a given obstacle coverage, what is the appropriate number of samples?*. As indicated by Figure 8, it is desirable to use the minimum number of samples, N_s , while still achieving acceptable solution cost, as this requires the minimum computation. Since the data given in Table 1 only represents a single obstacle coverage, a second test campaign was run to determine the necessary sample count as a function of obstacle coverage. Figures 9, 10, and 11 summarize the data from this second test campaign. Note that we referred to *approximate* obstacle coverage which is measured as the ratio of obstacle volume to unobstructed workspace volume. This value may be greater than one because obstacles were placed at random and overlapping volumes were double counted.

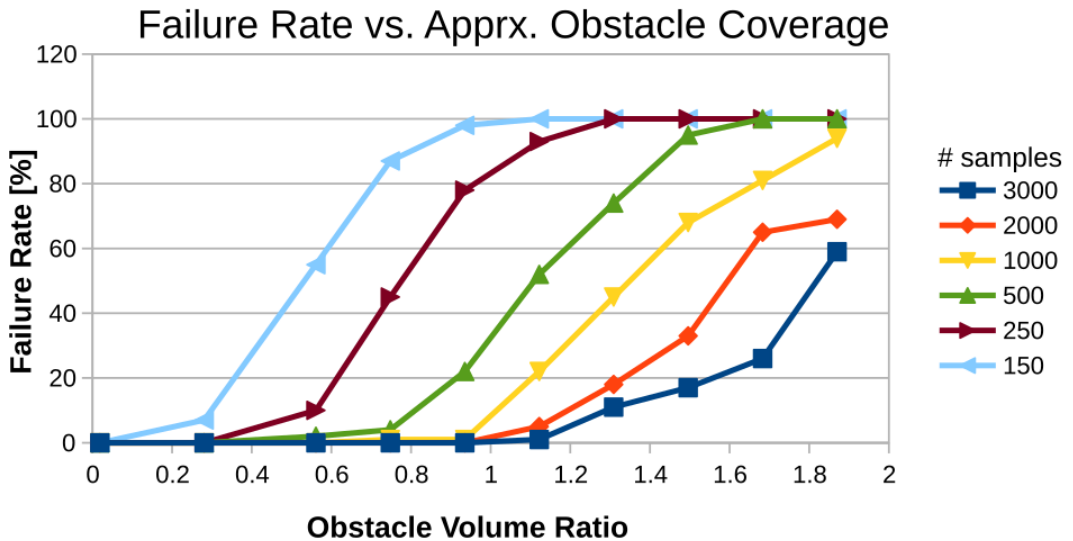


Figure 9. Rate of failure to find solution as a function of approximate obstacle coverage for a range of sample sizes.

We immediately see several trends in the data that we expect. First, Figure 9 shows that as the obstacle coverage increases, we must use larger sample numbers to prevent planner failure. Lower sample numbers, $N_s < 500$, quickly rise to 100% failure with increasing obstacle coverage. Note that for sample counts of $N_s = \{1000, 2000, 3000\}$, the curves diverge from 0% failure at roughly the same obstacle volume ratio. Therefore, $N_s = 1000$ is a favorable sample count because higher sample counts give no better guarantees for 0% failure at higher obstacle coverage.

Figure 10 gives average cost of a solution trajectory as a function of obstacle coverage and sample count. We see two expected trends: solution cost increases with increasing obstacle coverage and decreases with increasing samples

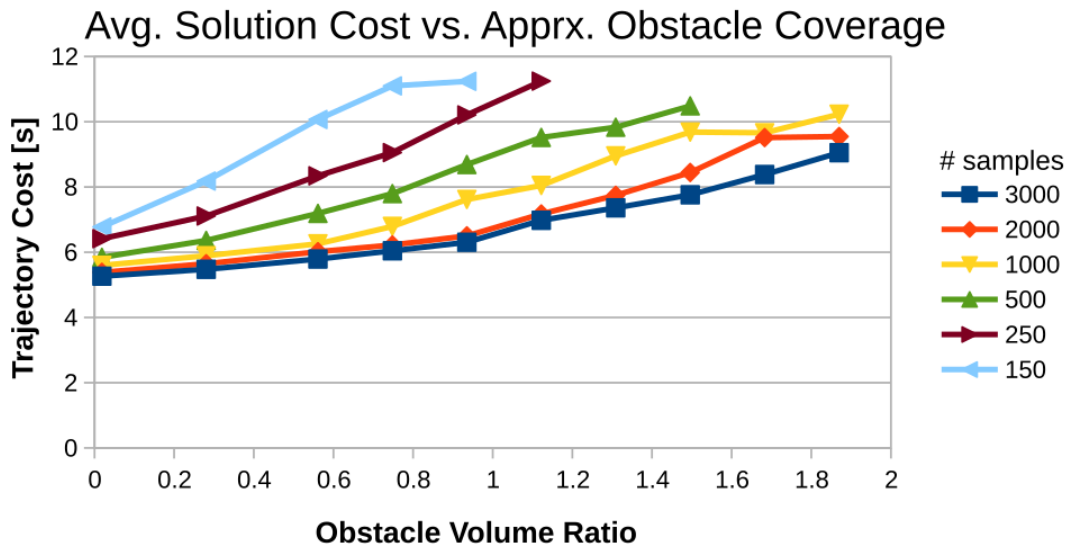


Figure 10. Average solution trajectory cost as a function of approximate obstacle coverage for a range of sample sizes.

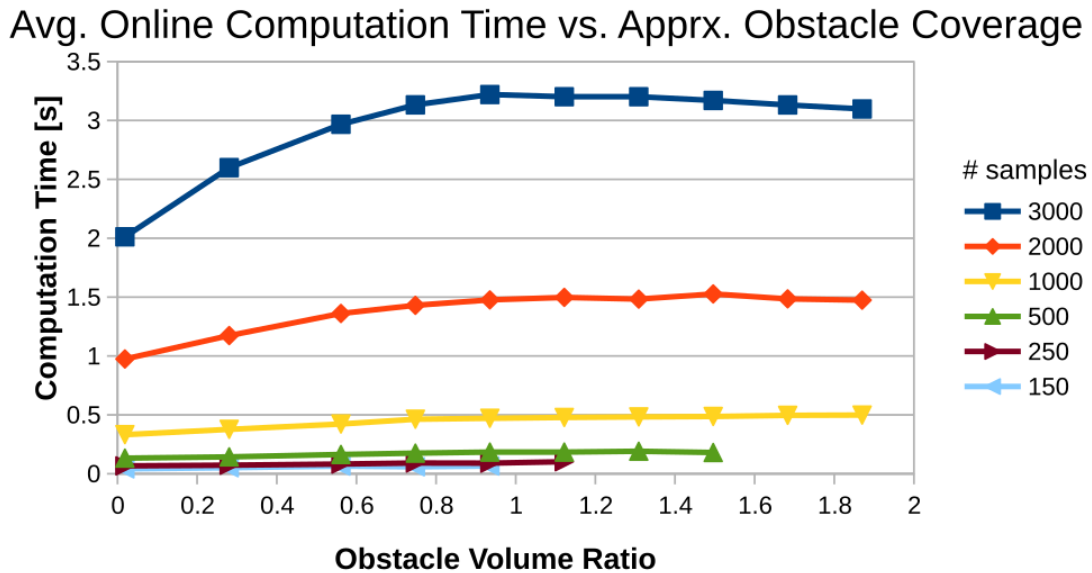


Figure 11. Average computation time as a function of approximate obstacle coverage for a range of sample sizes.

count (as was indicated in Figure 7). We also see that there is marginal improvement in solution cost beyond a sample count of 2000.

Figure 11 gives the online computation time as a function of sample count and obstacle coverage. Again we see the expected trends that computation time increases with increasing obstacle count and with increasing sample count. In more detail, we see that computation time roughly doubles for each tier of sample counts. This leads to large increases in computation time for sample counts greater than 1000. Based on this observation, plus the observation that there is marginal improvement in solution cost beyond $N_s = 2000$, plus the observation that $N_s = \{1000, 2000, 3000\}$ all diverge from 0% failure at the same obstacle coverage, we assert that $N_s = 1000$ is the best suited sample count for our physical experiments. Figure 11 shows that computation times for $N_s = 1000$ are less than 0.5 seconds, even in the worst case.

The simulation test campaign verifies that real-time planning framework achieves computation times of well below 1 second - typically on the order of 0.1 second with 0.5 second as a worst case - for a wide range of obstacle coverage. The test campaign also gives us the heuristic of $N_s = 1000$ as an acceptable sample count for the indoor environments and obstacle configurations considered in this paper. Now we test the effectiveness of the framework on a physical system navigating dynamic obstacles.

V.B. Experimental Flight Setup

The real-time framework is demonstrated on a Pixhawk autopilot flown on a DJI F-450 and F-330 frame. Positioning information is provided by a Vicon motion tracker with data streamed to the quadrotor via a Wifly RN-XV module. Currently the motion planning and path smoothing computations are run in MATLAB/C++ on a single-threaded Intel Core i7-4790K CPU. The final trajectory is transmitted to the Pixhawk for low-level flight control. This communication structure is represented in Figure 12. Table 2 gives detailed information on the computational platform and programming language for each of the major components of the framework discussed in Section IV. Future work will convert all portions of the online phase (see Alg. 2) to C++ to be run on an embedded processor on the quadrotor.

Table 2. Computational platform and programming language for the major components of the real-time framework.

Process	Reference	Processor	Language
localization	NA	workstation	C++
precomputations	IV	workstation	MATLAB
neighborhood estimation	IV.B	workstation	MATLAB
OBVP solutions	IV.A	workstation	MATLAB
sampling-based planning	IV.C	workstation	C++
min-snap smoothing	IV.D	workstation	MATLAB
flat-to-nonlinear mapping	IV.E	Pixhawk	C/C++
flight control	IV.F	Pixhawk	C/C++

The quadrotor is navigating an indoor environment with dimensions of approximately $3\text{m} \times 4\text{m} \times 3\text{m}$. The framework was tested on a range of obstacle sets, two of which are discussed in detail in Section V.C.

V.C. Experimental Flight Results

The real-time kinodynamic planner was successfully demonstrated in a campaign of flight tests. The test campaign was executed in the indoor environment of the Autonomous Systems Laboratory at Stanford University. During the campaign the quadrotor utilized the real-time planner to navigate a set of static and dynamic obstacles. Netting was hung from the ceiling to create maze-like environments while a human-subject would swing objects to create dynamic obstacles.

Figure 13 gives a timelapse of the most basic flight test performed: The quadrotor navigating a set of parallel walls with no dynamic obstacles present. The walls are arranged to create a z-shaped corridor 1.5m in width. This test acted as the first validating experiment for the real-time kinodynamic planner. The solution used 500 sampled states and required 0.313 seconds of online computation time. This test also demonstrated the agility of the quadrotor platform as indicated by the banged-turns as it rounded the corners. Building from this initial experiment, originally presented in Allen and Pavone [20], the planning code was optimized to further reduce computation times and dynamic obstacles were introduced.

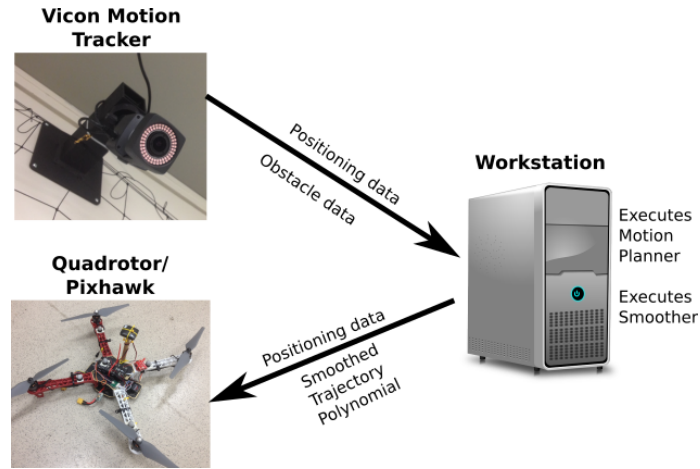


Figure 12. Communication/computation structure for flight tests.

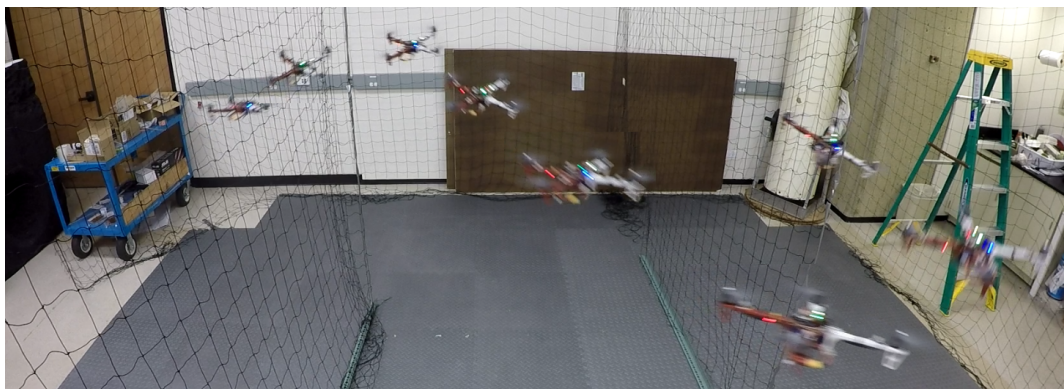


Figure 13. Timelapse of quadrotor navigating static obstacles.

In the first physical experiments with dynamic obstacles, shown in a sequence of images in Figure 14, the autonomous quadrotor is presented with a single obstacle in between its start state and its goal region. This creates two doors, each roughly one meter in width, from which the quadrotor can "choose" to navigate. When the real-time planner completes, the quadrotor begins executing the trajectory through the nearest of the two doors. Upon nearing the door, a human subject enters and presents a dynamic obstacle; in this demonstration the obstacle is the point of a fencing blade which is numerically expanded to a sphere with radius equal to the arm length of the quadrotor. The human subject continues to approach the quadrotor, causing it to be "pushed back" due to the reactive controller (see Section IV.F), until the existing trajectory is completely obstructed and replanning is initiated. Figure 15 shows the moment of replanning along with the solution provided by the real-time planning framework. Due to the proximity to the initially chosen door, the quadrotor executes three planning cycles that attempt to navigate the initial door and the dynamic obstacle. Since the dynamic obstacle is acting advicarially, always obstructing the chosen trajectory, this continues until the quadrotor is forced to a point where the second door becomes the optimal solution and the quadrotor navigates to the goal region without further obstruction from the human subject.

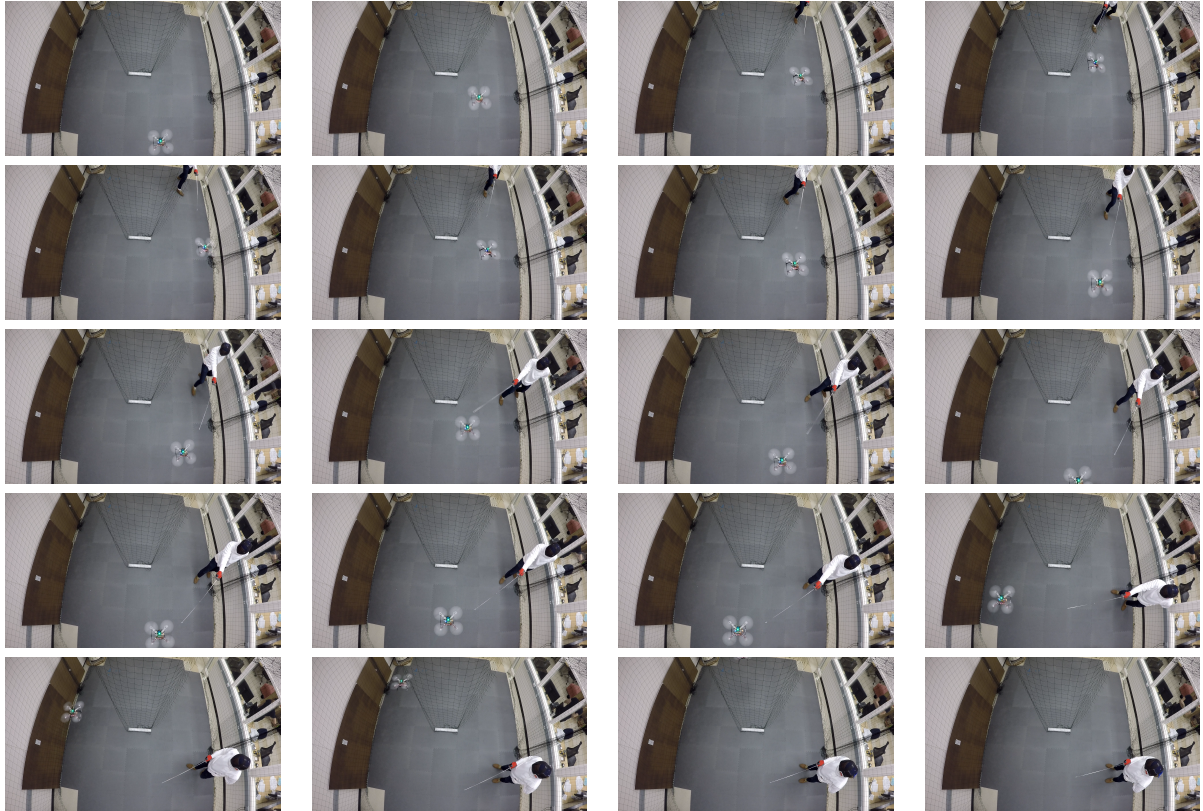


Figure 14. Sequence of images, in order from left to right and down, showing the quadrotor navigating the two-door environment with a human adversary obstructing one door using a fencing blade. The quadrotor initially attempts to navigate the door on the right. A human subject can be seen entering and obstructing the trajectory, causing the quadrotor to be "pushed back" due to the reactive controller. After several replanning events that attempt to navigate the door on the right, all of which are obstructed by the human subject, the left door eventually becomes the optimal solution which is determined by the real-time framework and subsequently executed by the quadrotor.

Figure 16 gives a second scenario where the autonomous quadrotor is tasked with navigating a parallel-walled maze with a corridor of roughly 1.5m in width. Again, a human subject introduces a set of dynamic obstacles to force online recomputation of the motion plan. During this demonstration the dynamic obstacles are presented immediately before the quadrotor rounds a corner, causing an abrupt replanning cycle that navigates over- and between the dynamic obstacles and the wall. Because the human subject does not continue to act advicarially in this case, only a single recomputation of the motion plan is necessary.

Figures 15 and 16 show that the online computation times for planning are on the order of 1/4 of a second.

V.D. Discussion

A primary goal of this work, the goal that is implied by the second motivating question in Section I, was to prove that the entire planning framework can be executed in a real-time environment. As shown in Figures 15 and 16, we achieve

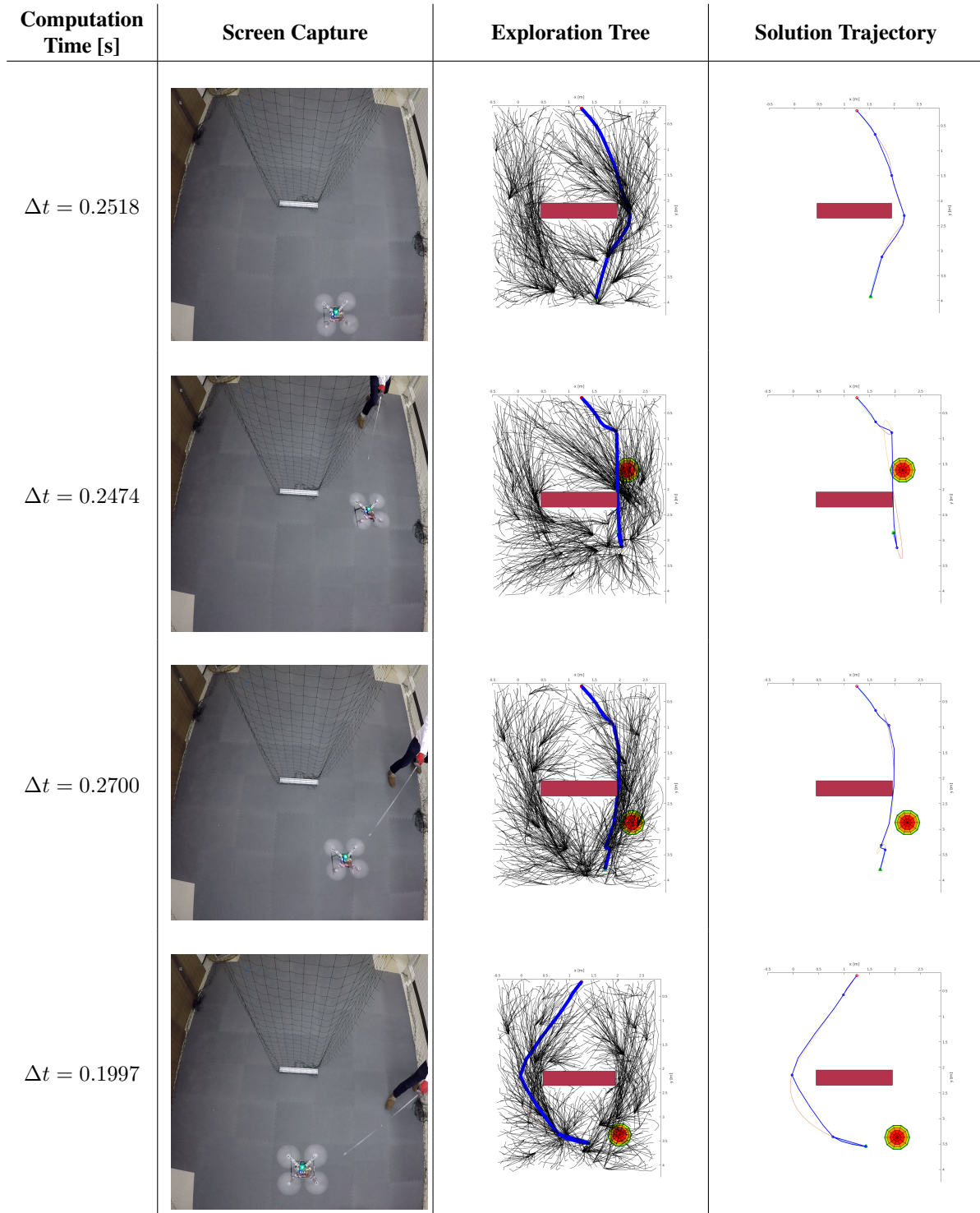


Figure 15. Time sequence of real-time planning in "two door" environment with static and dynamic obstacles. Column 1 gives the online computation time for the planning event. Column 2 gives screen capture of the moment of replanning. Column 3 gives the tree explored during replanning with the preliminary solution in blue. Column 4 gives the preliminary planning solution and the smoothed trajectory. Obstacles are represented by red rectangles or spheres

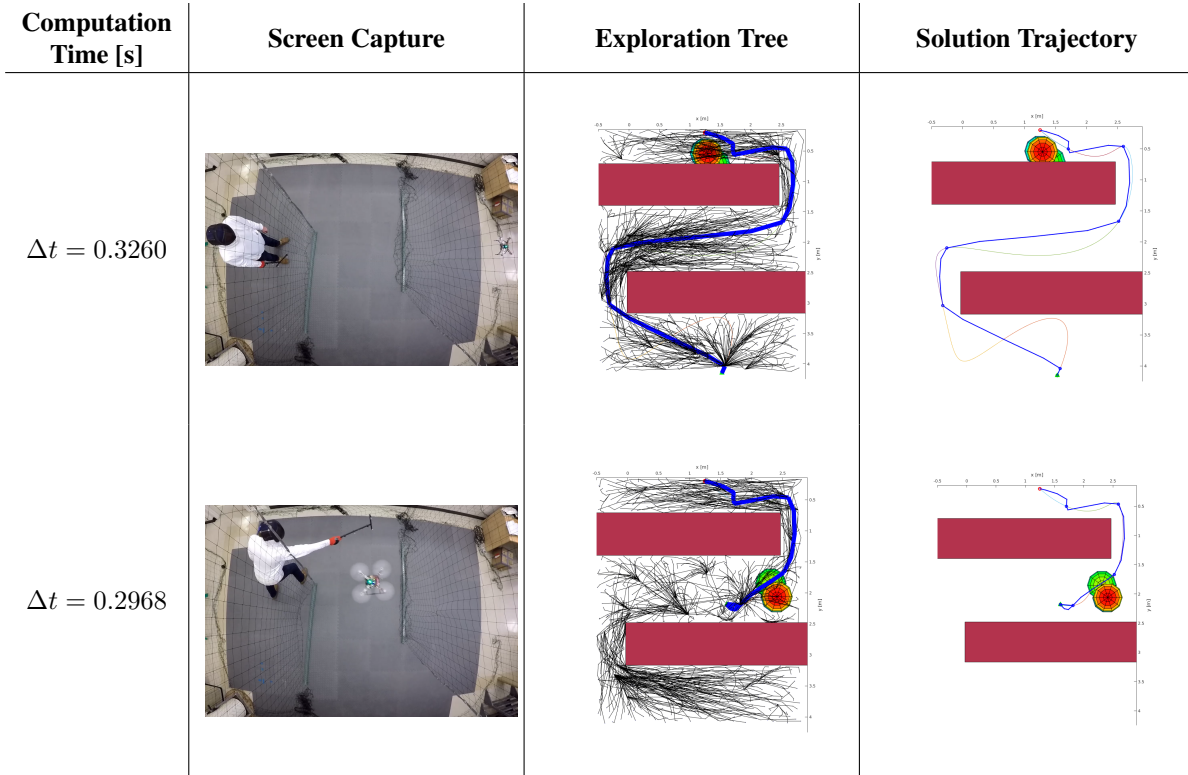


Figure 16. Time sequence of real-time planning in "maze" environment with static and dynamic obstacles. Column 1 gives the online computation time for the planning event. Column 2 gives screen capture of the moment of replanning. Column 3 gives the tree explored during replanning with the preliminary solution in blue. Column 4 gives the preliminary planning solution and the smoothed trajectory. Obstacles are represented by red rectangles or spheres

online computation times between 0.20 sec and 0.33 sec for 1000 sampled nodes. These computation times are in good agreement with those presented in Section V.A which ranged from 0.11 sec to 0.5 sec for comparable sample counts. The difference in computation times between simulated and physical experiments are due to differing obstacle sets (simulated tests being more densely obstructed) and additional computational tasks for physical experiments (e.g. communication of solution trajectories). To better understand the breakdown of computation time during physical experiments, Table 3 gives the percentage of computation time for separate tasks in the planner for a range of sample counts.

Table 3. Computation time breakdown for the Real-Time Kinodynamic Framework for differing numbers of sampled states

# of Samples	Neighbor Classifier [%]	Neighbor OBVPs [%]	Kino-FMT* [%]	Smoothing [%]	Comms [%]
500	6.42	37.73	9.43	30.43	25.29
1000	5.31	41.01	13.60	32.70	4.24
2000	4.56	41.65	19.81	26.40	3.38
3000	3.08	53.69	29.74	9.65	1.63

Referring to Table 3, the computation time is broken down into percentages for the major components of the framework: neighborhood classification for the terminal states (see Section IV.B); neighborhood OBVP solutions for the terminal states (see Section IV.A); sampling-based motion planning (see Section IV.C); path smoothing to generate a minimum-snap, dynamically feasible trajectory (see Section IV.D); and communication (see Section V.B). We see that the majority of the computation time is consumed by the solution of optimal boundary value problems between the terminal states, x_{init} and the samples in $\mathcal{X}_{\text{goal}}$, and their estimated neighborhoods. This result exemplifies the motivation to minimize the number of online OBVPs to be solved. For the double integrator model of the quadrotor, the average OBVP solution time is 0.0235 seconds per OBVP solution. In comparison, the average NearSVM classification time is 1.95×10^{-5} seconds per classification; roughly 1200 times, or three orders of magnitude, faster than OBVP solution. This rapid approximation of neighborhood sets as –opposed to explicit determination via OBVP solutions– is the

critically enabling component for real-time implementation.

To compare the computation times we achieved to those presented in the existing literature, Webb and van den Berg simulate an almost identical problem; however they do not perform any path smoothing or communication to a physical quadrotor [16]. With 1000 sampled states Webb and van den Berg’s solution takes 51.603 seconds; *i.e.* $\sim 150x$, or 2 orders of magnitude, slower than the technique presented here. Richter et. al. do not state the computation time for motion planning demonstrated in their work [7]. They do, however, give the computation time for a simplified, 2-dimensional problem that incorporates geometric path planning and minimum-snap path smoothing. Richter’s simplified, 2D planning problem takes 3 seconds of computation time; *i.e.* $\sim 9.1x$, or 1 order of magnitude, slower than the slowest physical experiment computation time presented here. Therefore the real-time kinodynamic framework demonstrates a significant reduction in computation time when compared to existing techniques.

Frazzoli et. al. boasts the most impressive computation times with sub-second execution for the similar, but not identical, helicopter system navigating static spherical objects [5]. Computation times for dynamic obstacles rise to 10s of seconds for a parallel wall obstacle set. Therefore we again see our method produce roughly 2 orders of magnitude improvement in computation time when compared to existing techniques for dynamic obstacles. Direct comparison with Frazzoli’s work is more difficult because it only seeks feasible trajectories, not necessarily optimal ones. The work employs only a small set of motion primitives - avoiding the solution to online OBVPs all together - to achieve path planning. Restricting trajectories to a small set of predefined maneuvers limits the technique’s ability to handle novel, complex, or even pathological obstacle environments.

We note here that our physical demonstrations were not infallible; roughly 50% of experiments ended in some form of a crash. These failures were found to be due to two factors: poor system identification of the quadrotor leading to inaccurate dynamic parameters in the flight controller (see Section IV.F), and loss of positioning data due to exiting Vicon coverage. Both of these failure modes were outside the scope of this work which was solely focused on developing the real-time planning framework. These failure modes, do however, motivate future work: advanced system identification for improved controller performance and robust, onboard estimation/localization to eliminate reliance on a motion capture system.

V.E. Results for Machine Learning of Reachable Sets

Table 4. Feature vector for neighbor determination of the double integrator quadrotor model.

x_1	x_2	$ \Delta x $	$(\Delta x)^2$	$(\Delta x)^3$	$\sqrt{(\Delta x)^2 + (\Delta y)^2 + (\Delta z)^2}$
y_1	y_2	$ \Delta y $	$(\Delta y)^2$	$(\Delta y)^3$	$\sqrt{(\Delta \dot{x})^2 + (\Delta \dot{y})^2 + (\Delta \dot{z})^2}$
z_1	z_2	$ \Delta z $	$(\Delta z)^2$	$(\Delta z)^3$	$\sqrt{(\Delta x)^2 + (\Delta y)^2 + (\Delta z)^2 + (\Delta \dot{x})^2 + (\Delta \dot{y})^2 + (\Delta \dot{z})^2}$
\dot{x}_1	\dot{x}_2	$ \Delta \dot{x} $	$(\Delta \dot{x})^2$	$(\Delta \dot{x})^3$	
\dot{y}_1	\dot{y}_2	$ \Delta \dot{y} $	$(\Delta \dot{y})^2$	$(\Delta \dot{y})^3$	
\dot{z}_1	\dot{z}_2	$ \Delta \dot{z} $	$(\Delta \dot{z})^2$	$(\Delta \dot{z})^3$	

Due to the reliance on machine-learning of neighbor sets, it is important to determine the classification accuracy of the NearSVM algorithm. In this work we apply the NearSVM algorithm (see Section IV.B) to the control-penalized double integrator system presented in Section IV.A. The state space of the double integrator system in Equation 4 is 6-dimensional. The two boundary values for an OBVP are concatenated into a 12-dimensional attribute vector, given as \mathbf{p} in Equation 10. The feature vector is a 33-element vector, given in Table 4, composed of nonlinear mappings of elements from the attribute vector. A third order kernel function is chosen; therefore $p = 3$ in Eqn. (11). For training and testing of the SVM classifier, 50000 OBVPs are solved from randomly selected pairs of sampled states during the offline computation phase. A neighbor radius, or cost threshold, is chosen as the 10th quantile of all OBVP costs; which for this test campaign evaluated to neighbor cost threshold of roughly 0.69 seconds. In other words, for a given state, roughly 10% of all other states are within 0.69 seconds as measured by a minimum-time optimal control problem. To train the SVM classifier, $N_{\text{train}} = 20000$ of the 50000 OBVP solutions were used with the 0.69 second cost threshold. On average less than one training error occurred per the 20000 training examples.

The algorithm was tested against 30000 additional OBVP examples to ensure that the SVM was not *over-trained* to the training set ^e. The average testing error was under 3%, well within the acceptable tolerance for the purpose of this work and a marked improvement over the author’s prior work on machine learning of cost-limited reachable sets [19]. Table 5 gives the training and testing results. A ‘positive’ indicates that NearSVM classified the OBVP example

^eTypically the training set would be much larger than the testing set, but due to convergence issues while training, the training set was reduced and the remainder of OBVP examples was dedicated to the testing set.

Table 5. Training and testing accuracy of machine-learning-based neighborhood classification algorithm

# Training Examples	Avg. # Training Errors	# Testing Examples	Avg. # True Positives	Avg. # True Negatives	Avg. # False Positives	Avg. # False Negatives	Avg. Testing Error [%]
20000	0.6	30000	2693	26600.6	371.8	334.6	2.35

as within the cost threshold, and a ‘negative’ indicates a classification of the OBVP outside of the cost threshold. The number of true positives is roughly 10% of the number of true negatives; as expected with the 10th quantile cost threshold. The average number of false positives and false negatives are approximately equal indicating that the classifier is not biased toward one classification^f.

The information given in Table 5 only tells us the rate of neighborhood classification error, it does not tell us where in the state space these misclassifications occur. To form a deeper understanding of where/why misclassification of neighbors occur, we illustrate the NearSVM results with a simplified case. Figure 17 presents a set of trials for the neighborhood classifier when compressed to 2 spacial dimensions and one velocity dimensions. Each trial, represented by its own image in Figure 17, attempts to classify the reachable neighborhood of an initial state. For each trial, the initial state is the origin with a y-velocity ranging from 0 m/s to 14 m/s. The final states for each classification are spread across the xy-axes and all have a final velocity of zero. The neighborhood cost threshold is 2.178 seconds which corresponds to the 10th quantile of costs for this set of training data.

The reachability of each final state is assessed by solving an OBVP, as discussed in Section IV.A, between the initial state and each final state. Reachable states are indicated in blue circles and non-reachable are indicated in black triangles. The machine learning algorithm, NearSVM, is then applied to estimate reachability. Misclassification of reachability, whether it be a false-positive or false-negative, is indicated by a red star.

As expected, Figure 17 shows that the true reachable set shifts further along the y-axis as the initial velocity in the y-direction increases. We also see that misclassification of reachability always occurs on the boundary between the reachable and non-reachable sets. This is a desirable result for a well-trained algorithm. A poorly-trained algorithm would make classification errors well within the reachable or non-reachable sets. If a poorly trained neighborhood classifier were used in the real-time planning framework, we would end up solving OBVPs for states that are well outside of neighborhood - likely leading to collisions with obstacles, increasing computation time - or fail to recognize nearby states, thus increasing solution cost of our trajectory.

It is important to note that an analytical solution exists for the reachable set of the control penalized double integrator [16]. The question is then, why would you use the machine learning approximation for reachable sets when an analytical solution exists? This question lies at the balance point between the two motivating questions presented in Sec I. While we want to demonstrate real-time planning for a quadrotor, we also want to validate a planning framework that is more applicable to a more general set of dynamical systems. Since an arbitrary dynamical system cannot be expected to have an analytical solution for reachable sets, we maintain the use of the machine learning approach in effort to validate it in physical experiments.

VI. CONCLUSIONS

This work presents a full-stack, quadrotor planning architecture that is shown to reduce online computation times below one second; several orders of magnitude faster than techniques presented in existing literature. This is arguably one of the first - if not the first - demonstration of truly real-time kinodynamic planning on a quadrotor system navigating an obstructed environment. Going even further, we have successfully implemented such framework in a dynamic environment with moving obstacles. The drastic improvement in online computation time is achieved by reducing the number of online optimal boundary value problems to be solved to constant order. The reduction to constant order OBVP solutions is enabled by machine learning estimates of reachability sets for a dynamical system.

While this work is targeted at demonstration of real-time planning for a quadrotor system, much of the presented framework remains generally applicable to motion planning for an arbitrary dynamical system. Therefore the presented work is relevant for a wide range of planning and control problems.

Further work will validate and extend these results. All components of the planning framework will be translated

^fFor example, we could use a trivial classifier that only predicted negatives and it would return a testing error of 10% because only 10% of cases are positive. This would actually constitute an acceptable rate of classification error if it were not for the fact that all errors would be false negatives as the classifier is trivial. Therefore a well trained classifier should not be biased toward one type of error.

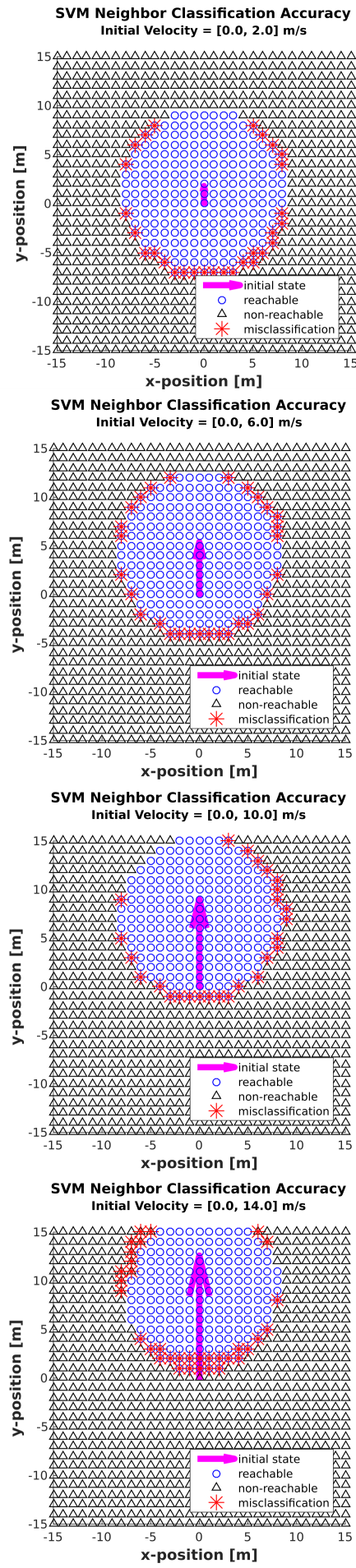
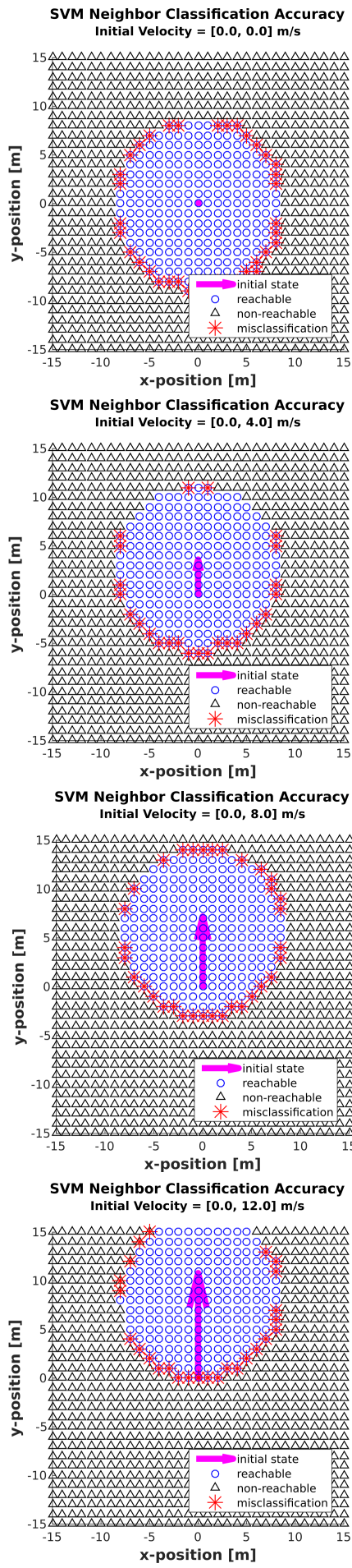


Figure 17. Simplified, 2-dimensional reachable set classification. For all cases, the start state is at the origin with an initial velocity in the y-direction. The final states all have a velocity of zero. [discuss training set](#)

to C/C++ and run on an embedded processor flown on the quadrotor. While the processing power on an embedded system will be diminished when compared to the workstation used in this paper, the translation from MATLAB to C/C++ is expected to roughly balance the effect; therefore computation times are not expected to change significantly. The localization and mapping that is currently achieved with the Vicon motion capture system will be integrated into the quadrotor system using a range of visual, laser, and ultrasonic sensors. In this way, real-time localization and planning will be achieved on a fully self-contained platform. Enhanced system identification will be performed on the quadrotor system, improving flight control and allowing for even more agile interactions with obstacles.

In the work presented here, we've assumed perfect knowledge of the quadrotor and obstacles states and dynamics. This simplifying assumption will be removed in future work that will involve planning under uncertainty. To handle the additional computational complexity of planning under uncertainty, a parallelized planning algorithm will be executed on an onboard GPU.

Beyond quadrotor application, we hope to demonstrate the real-time kinodynamic planning framework on a wide range of dynamical systems such as spacecraft, cars, marine and submarine vehicles, cranes, etc. Furthermore, this work can be extend from single agent to multi-agent systems. Of particular interest is the possibility of emergent behavior due to many agents selfishly solving their own planning problem while avoiding collisions with other agents. Finally game theory could be applied so that robotic agents can model dynamic obstacles as advisories for more sophisticated avoidance maneuvers.

The code base for this work can be found at: <https://github.com/StanfordASL/KinoFMT.git>

References

- ¹ Gabriel M Hoffmann, Haomiao Huang, Steven L Waslander, and Claire J Tomlin. Quadrotor helicopter flight dynamics and control: Theory and experiment. In *Proc. of the AIAA Guidance, Navigation, and Control Conference*, volume 2, 2007.
- ² Samir Bouabdallah, Andre Noth, and Roland Siegwart. PID vs LQ control techniques applied to an indoor micro quadrotor. In *Intelligent Robots and Systems, 2004.(IROS 2004). Proceedings. 2004 IEEE/RSJ International Conference on*, volume 3, pages 2451–2456. IEEE, 2004.
- ³ Markus Hehn and Raffaello D’Andrea. A flying inverted pendulum. In *Robotics and Automation (ICRA), 2011 IEEE International Conference on*, pages 763–770. IEEE, 2011.
- ⁴ S. M. LaValle. Motion planning: Wild frontiers. *IEEE Robotics Automation Magazine*, 18(2):108–118, 2011.
- ⁵ E. Frazzoli, M. A. Dahleh, and E. Feron. Real-time motion planning for agile autonomous vehicles. *AIAA Journal of Guidance, Control, and Dynamics*, 25(1):116–129, 2002.
- ⁶ Peter Leven and Seth Hutchinson. A framework for real-time path planning in changing environments. *The International Journal of Robotics Research*, 21(12):999–1030, 2002.
- ⁷ C. Richter, A. Bry, and N. Roy. Polynomial Trajectory Planning for Aggressive Quadrotor Flight in Dense Indoor Environments. In *International Symposium on Robotics Research*, 2013.
- ⁸ Charles Richter, Adam Bry, and Nicholas Roy. Polynomial Trajectory Planning for Quadrotor Flight. In *International Conference on Robotics and Automation*, 2013.
- ⁹ D. Mellinger and V. Kumar. Minimum Snap Trajectory Generation and Control for Quadrotors. In *Proc. IEEE Conf. on Robotics and Automation*, pages 2520–2525, 2011.
- ¹⁰ S. Karaman and E. Frazzoli. Sampling-based algorithms for optimal motion planning. *International Journal of Robotics Research*, 30(7):846–894, 2011.
- ¹¹ Koushil Sreenath, Taeyoung Lee, and Vipin Kumar. Geometric control and differential flatness of a quadrotor UAV with a cable-suspended load. In *Decision and Control (CDC), 2013 IEEE 52nd Annual Conference on*, pages 2269–2274. IEEE, 2013.
- ¹² Daniel Mellinger, Nathan Michael, and Vijay Kumar. Trajectory generation and control for precise aggressive maneuvers with quadrotors. *The International Journal of Robotics Research*, page 0278364911434236, 2012.
- ¹³ Ian D Cowling, Oleg A Yakimenko, James F Whidborne, and Alastair K Cooke. Direct method based control system for an autonomous quadrotor. *Journal of Intelligent & Robotic Systems*, 60(2):285–316, 2010.
- ¹⁴ Ian D Cowling, Oleg A Yakimenko, James F Whidborne, and Alastair K Cooke. A prototype of an autonomous controller for a quadrotor UAV. In *Control Conference (ECC), 2007 European*, pages 4001–4008. IEEE, 2007.

- ¹⁵ Y Bouktir, M Haddad, and T Chettibi. Trajectory planning for a quadrotor helicopter. In *Control and Automation, 2008 16th Mediterranean Conference on*, pages 1258–1263. IEEE, 2008.
- ¹⁶ D. J. Webb and J. van den Berg. Kinodynamic RRT*: Optimal Motion Planning for Systems with Linear Differential Constraints. In *Proc. IEEE Conf. on Robotics and Automation*, pages 5054–5061, 2013.
- ¹⁷ Benoit Landry. Planning and Control for Quadrotor Flight Through Cluttered Environments. Master’s thesis, Massachusetts Institute of Technology, 2015.
- ¹⁸ Slawomir Grzonka, Giorgio Grisetti, and Wolfram Burgard. A Fully Autonomous Indoor Quadrotor. *Robotics, IEEE Transactions on*, 28(1):90–100, 2012.
- ¹⁹ Ross Allen, Ashley Clark, Joseph Starek, and Marco Pavone. A Machine Learning Approach for Real-Time Reachability Analysis. In *IEEE/RSJ Int. Conf. on Intelligent Robots & Systems*, pages 2202–2208, Chicago, IL, September 2014.
- ²⁰ Ross Allen and Marco Pavone. Toward a Real-Time Framework for Solving the Kinodynamic Motion Planning Problem. In *Proc. IEEE Conf. on Robotics and Automation*, Seattle, WA, May 2015.
- ²¹ Ross Allen and Marco Pavone. A Real-Time Framework for Kinodynamic Planning with Application to Quadrotor Obstacle Avoidance. In *AIAA Conf. on Guidance, Navigation and Control*, San Diego, CA, January 2016. Submitted.
- ²² John Schulman, Jonathan Ho, Alex Lee, Ibrahim Awwal, Henry Bradlow, and Pieter Abbeel. Finding Locally Optimal, Collision-Free Trajectories with Sequential Convex Optimization. In *Robotics: Science and Systems*, volume 9, pages 1–10. Citeseer, 2013.
- ²³ S. Lavalle. *Planning Algorithms*. Cambridge University Press, 2006.
- ²⁴ Taeyoung Lee, Melvin Leok, and N Harris McClamroch. Nonlinear Robust Tracking Control of a Quadrotor UAV on SE (3). *Asian Journal of Control*, 15(2):391–408, 2013.
- ²⁵ S. M. LaValle and J. J. Kuffner. Randomized Kinodynamic Planning. *International Journal of Robotics Research*, 20(5):378–400, 2001.
- ²⁶ Lucas Janson, Edward Schmerling, Ashley Clark, and Marco Pavone. Fast Marching Tree: A Fast Marching Sampling-Based Method for Optimal Motion Planning in Many Dimensions. *International Journal of Robotics Research*, 34(7):883–921, 2015.
- ²⁷ Yanbo Li, Zakary Littlefield, and Kostas E Bekris. Asymptotically optimal sampling-based kinodynamic planning. *arXiv preprint arXiv:1407.2896*, 2014.
- ²⁸ I Michael Ross and Fariba Fahroo. Issues in the real-time computation of optimal control. *Mathematical and computer modelling*, 43(9):1172–1188, 2006.
- ²⁹ E. Schmerling, L. Janson, and M. Pavone. Optimal Sampling-Based Motion Planning under Differential Constraints: the Drift Case with Linear Affine Dynamics. In *Proc. IEEE Conf. on Decision and Control*, 2015.
- ³⁰ Shuzhi S. Ge and Yun J Cui. Dynamic motion planning for mobile robots using potential field method. *Autonomous Robots*, 13(3):207–222, 2002.
- ³¹ Edward Schmerling, Lucas Janson, and Marco Pavone. Optimal Sampling-Based Motion Planning under Differential Constraints: the Drift Case with Linear Affine Dynamics (Extended Version). Available at <http://arxiv.org/abs/1405.7421/>, May 2015.
- ³² D. M. Stipanovic, I. Hwang, and C. J. Tomlin. Computation of an Over-Approximation of the Backward Reachable Set Using Subsystem Level Set Functions. *Dynamics of Continuous Discrete and Impulsive Systems*, 11:397–412, 2004.
- ³³ Christopher M Bishop. *Pattern recognition and machine learning*. Springer, 2006.
- ³⁴ E. Schmerling, L. Janson, and M. Pavone. Optimal Sampling-Based Motion Planning under Differential Constraints: the Driftless Case. In *Proc. IEEE Conf. on Robotics and Automation*, pages 2368–2375, 2015.